A Dissertation for the Degree of Doctor of Philosophy in Astronomy,

Space Science and Geology

Investigation of topographic and object characteristics of terrestrial impact craters based on remote sensing approaches

Department of Astronomy, Space Science and Geology

Graduate School

Chungnam National University

By

HABIMANA Emmanuel

Advisor Jaehyung Yu

February, 2024

Investigation of topographic and object characteristics of terrestrial impact craters based on remote sensing approaches

Advisor: Jaehyung Yu

Submitted to the Graduate School

in Partial Fulfillment of the Requirements

for the Degree of

Doctor of Philosophy in Astronomy, Space Science and Geology

October, 2023

Department of Astronomy, Space Science and Geology

Graduate School

Chungnam National University

By

HABIMANA Emmanuel

To Approve the Submitted Dissertation for the Degree of Doctor of Philosophy in Astronomy, Space Science and Geology

By HABIMANA Emmanuel

Title: Investigation of topographic and object characteristics of terrestrial impact craters based on remote sensing approaches

December, 2023

Committee Chair Yongjae Yu (인 or Sign)

Committee Jaehyung Yu (인 or Sign)

Committee Jeong-Hyun Lee (인 or Sign)

Committee Saro Lee (인 or Sign)

Committee Yun Gon Lee (인 or Sign)

Graduate School

Chungnam National University

LIST OF CONTENTS

LIST OF FIGURES

LIST OF TABLES

PROLOGUE

Impact craters are important landforms formed by the collision of hypervelocity celestial objects such as asteroids or comets with the planet's surface. The formation of impact craters involves three main stages including contact and compression, excavation, and modification that reshape the Earth's crust and leave the circular-shaped topographic imprints on the planet's surface. The processes involved in crater formation depend on several factors including the energy of the impactor, target lithology, and rheological condition of target rocks that lead to small or large impact structures.

Impact cratering has been found as an important geological record that assists in quantifying impact flux in geological time scale, and reveals the evolution of planets, and other celestial objects. Impact crater science helps also to date the geological phenomena, and come up with a chronological sequence of planetary events. In addition, the impact cratering induces an impressive geological landform that plays a great role in geo-tourism development and geological heritage. Therefore, a substantial effort is made to explore and describe those remarkable and impressive landscapes based on various techniques such as remote sensing, geophysics, and geological surveys.

The exploration of impact craters included reconnaissance and conclusive stages. The stage of reconnaissance involves mainly remote sensing and geophysical surveys to describe the morphology of potential impact crater candidates and serve as a guide to the final conclusive stage. The conclusive stage aimed at identifying the mega-scales and macroscale evidence such as shatter cones and planar deformation features in shocked quartz via extensive geological surveys and laboratory experiments. Various techniques and impact crater detection algorithms are continuously developed to improve impact crater detection based on remote sensing data. Several automatic approaches have been mostly focused on extraterrestrial planets; however, few trials have been performed to detect terrestrial impact craters, were limited to few numbers in narrow diameters size. These limited the exploration of impact crater candidates in remote areas or areas of limited access.

The morphological expressions of extraterrestrial impact craters are more exposed to the surface which ease automatic detection compared to the terrestrial craters because of active

geological conditions of Earth's crust. In addition, most automatic crater detection algorithms that have been developed are based on pixels that might be easily affected by noise and have limitations in recognizing complex spatial features in heterogenous landscapes like Earth's surface. To contribute to the terrestrial impact crater exploration and overcome the limitation of pixel-based image analysis, Object-Based Image Analysis (OBIA) was executed in this study expecting the formation of circular segments around the circular morphology of impact craters. The OBIA is more convenient in the tasks of identifying or analyzing the relationship of spatial features such as landscapes, and urban mapping. The objects or segments of targeted features are formed via the multiresolution segmentation algorithm, where the size of the object depends on user-defined scale parameters. The global 30m/pixel resolution Shuttle Radar Topography Mission Digital Elevation Model (SRTM DEM) was the source of raster topography data in this study.

On the other hand, the impact crater morphometric studies divide the impact craters in three types including simple, complex, and transitional (basin). The pristine simple craters are indicated by sharp bowl-shaped depressions with a diameter size of ~ 2 km for sedimentary and ~4 km for crystalline. Typical pristine complex craters are mainly indicated by terraced wall, the central peak in crater floor and the size varies widely from around ~ 4 km in diameter. However, the transition craters have relatively flat floor bases compared to the simple craters and lack central pick rings. The transitional diameter is not an abrupt change, it even varies from one planetary body to another because of the gravitation force and rheology of target rocks. Presently, the size of known transitional terrestrial craters varies from 3 – 10 km. Discovering impact craters is a dynamic process, every decade several new impact craters are discovered, however, recognizing impact crater types is not straightforward in geological active conditions like Earth's crust, and post-impact craters processes including mass transport of crater wall, and sediment deposition layers usually confine central uplifts. The case example is Jeokjung Chogye Basin (JCB) in the Korean peninsula, South Korea, it has been recently confirmed as an impact crater, but the crater type is still unclear. To investigate the buried central uplift a complex and cost-effective geophysics surveys such as gravity, magnetic surveys, and drillings are mostly used to detect the densified peak rocks that emerge in sediment layers.

However, an environmentally friendly and spatial scale adaptation approach based on morphometric parameters analysis and test statistics could be an alternative user-friendly technique to provide a preliminary crater type of suspected impact craters. The morphometric parameters including rim diameter, floor diameter, wall width, and crater depth extracted from raster topographic data have been used to identify crater types on extraterrestrial bodies. Although the extraterrestrial impact craters are mostly well exposed, a similar approach could be used for less modified terrestrial impact craters. This study is generally aimed at introducing object oriented remote sensing approaches for detection of terrestrial impact craters, and identification of possible crater types at a preliminary exploration stage.

Therefore, this dissertation aims at providing the solution of five major specific problems.

i. Is there a possibility of detecting terrestrial impact craters based on object features rather than pixels signatures?
ii. What are the optimum scale parameters for impact craters segmentation?
iii. Are there important parameters that can improve craters detection from other similar features?
iv. Is there a possibility of distinguishing simple from complex terrestrial craters based on remote sensing approaches?
v. Can morphometric parameters identify the crater type of Jeokjung Chogye Basin, South Korea?

The possible solutions of the above-mentioned questions are examined in this dissertation. Chapter 1 deals with the three top questions (i–iii), and chapter 2 discusses bout two last questions (iv– v).

Chapter 1:

The impact craters are the most important geological features that display the circular or subcircular morphological depressions on the planetary's body surface. The morphological depressions can be observed to a certain extent with various multi-altitude platforms eg. satellites based on raster multispectral or topography data. Thus, it is nearly impossible to visualize the deeply eroded and buried craters via the surface remote sensing approaches. Many impact craters still need to be discovered, indeed the current confirmed impact craters are differently distributed around the world because of different levels of advanced technology and

investment in impact crater exploration. Although previous studies have attempted several crater detection algorithms, much attention was paid to extraterrestrial impact craters, and few attempts have been tested on a small number of terrestrial impact craters. The main constraint for terrestrial impact craters is the size variability and exposure level.

This chapter attempted to overcome the limitations of the size variability of terrestrial impact craters in complex geological conditions and reports the segmentation results conducted on raster topography satellite data covering a wide range of 0.88 – 100 km in diameter of impact craters. The multi-segmentation algorithm controls the size of segments or objects formed based on the size of scale parameters. The correlation estimating the relationship between scale parameters and the diameter size of impact craters was established. Moreover, the Random Forest object-oriented model classified 94 impact crater objects, 104 volcanic calderas, and 124 valley objects. The model was tested with other endogenic features like volcanic calderas exhibit circular depressions on the planet's surface, and valleys are commonly found features mostly associated with mountainous regions. Therefore, an object-based automatic crater detection model as a reconnaissance survey was developed, and parameters that played a major role in detecting impact craters from other features have been defined.

Chapter 2:

Several previous case-specific studies characterized different terrestrial impact crater types in terms of morphometric parameters. This gives an insight that morphometric parameters derived from remote sensing topographic data can provide a clue about the impact crater type of the suspected candidate without ultimate evidence from geophysical and drilling operations. Indeed, many studies used rim diameter, depth, floor diameter, wall width, etc., to distinguish a wide range of simple, complex, and transitional craters on the Moon, Mars, etc. This study was then conducted to test the significant difference between simple and complex terrestrial crater types in terms of morphometric parameters. Moreover, the newly discovered impact crater type in South Korea was inferred.

The impact crater research team in South Korea focused first on identifying the conclusive confirmation of Jeokjung Chogye Basin as an impact origin. However, studies aimed at identifying impact crater types associated with the Jeokjung Chogye Basin have not been conducted yet. Then, this study reports an approach to tracking the impact crater type of

JCB in terms of morphometric parameters. The test statistics investigated the significant difference between 11 simple craters and 38 complex craters. Furthermore, the association of JCB with either simple or complex was tested. In addition, the machine learning algorithm investigated the classifiability between the two types of impact craters and then classified the crater associated with JCB. Finally, we introduced the important variables for classifying the different crater types based on morphometric parameters. The research results are then summarized in the epilogue section.

CHAPTER 1. REMOTE SENSING BASED IMPACT CRATER DETECTION METHODS[1]

1.1. Introduction

Impact craters are paramount geological features in planet evolution and planetary sciences. They are formed by impacting asteroids, or comets with the planetary or moon's surface and modify the landscape of planetary leaving circular or sub-circular topographic imprints on the surface [1]. The various scales of circular topographic features are mainly driven by the energy level of the impactor, which can be observed by satellites [2]. Impact craters have become one of the important scientific focuses in the planetary science community as they host evidence for inference of understanding of space materials and planet of evolution [3]. Furthermore, they are crucial indicators related to space hazards causing secondary earthquakes and tsunamis [4]. Approximating impact crater ages is used to determine impact flux in the geological time scale and compare it with other geological events in Earth's evolution [5]. The geoscientists have therefore put a substantial effort into detecting and analyzing the impact crater's impressive landscapes based on diverse sources including space based remote sensing, ground based geophysical and geological data.

Impact craters are formed into three consecutive phases such as contact and compression, excavation, and modification [2, 10]. The contact and compression phase occur just when the impactor gets in contact with the target surface, and cause compression and deformation because of the high energy of the impactor, shock wave, and pressure expansion. The excavation phase happens because of the transfer of impactor energy to the target body and causes a digging up of a bowl-shaped cavity leading to the ejection of materials and the

[1]This chapter has been published by Emmanuel, H.; Yu, J.; Wang, L.; Choi, S.H.; Rwatangabo, D.E.R (2023). Object-Oriented Remote Sensing Approaches for the Detection of Terrestrial Impact Craters as a Reconnaissance Survey. *Remote Sens.2023,15*,3807. https://doi.org/ 10.3390/rs15153807

formation of a transient crater. The modification phase that produces the final shape of craters consists of the collapse of the transient crater wall, central uplift rebound, and the uplifted and fractured materials formed around the crater's circumference rim [2, 10].

The worldwide distribution of confirmed craters is biased by the extensive geological survey technology available in most developed countries. Indeed, most confirmed impact craters are concentrated in developed countries[6]. Kenkmann et al.[7] reported the uneven statistical distribution of 198 confirmed and 10 suspected impact craters, as follows: 65 in North America, 54 in Europe, 31 in Australia, 23 in Asia, 21 in Africa, and 14 in South America [7]. The regions with limited accessibility and lack of enough infrastructure cause the impact craters deficiency in many countries in Asia, South America, and Africa. Therefore, more impact craters can be possibly identified in those low-finding areas.

Identification of terrestrial impact craters consists of two-major exploration stages; preliminary and conclusive stages[8,9,10]. The first stage involves remote sensing, including topographic, optical, magnetic, or gravity surveys. The geophysical exploration played a major role especially in identification of deeply, submerged and buried impact structures [13,14]. The conclusive crater identification stages involve intensive geological surveys such as well-logging, geochemical analysis, lab analysis, and shock metamorphic experiments, and conclude the crater candidates as an impact origin by ultimate evidences (shatter cones and planar deformation features, etc..) [8,9,10]. Remote sensing can provide worldwide coverage of preliminary screening assessment of possible crater locations to narrowing down candidates based on satellite data [11,12]. It is therefore divided into three stage categories.

The first category uses Digital Elevation Models (DEMs) to outlines the geomorphological evidence of impact structures. The geomorphological characteristics such as crater rims and ring, shape and size of crater structures can be deduced from the DEMs[15,16]. The DEMs also can be used to define morphological indicators of confirmed impact craters from geological surveys [17,18,19]. In addition, the drainage networks related with crater

structures have been also investigated to outline the extent of the drainage basin [16]. The centrifugal or centripetal radial drainage, and concentric drainage patterns are mostly observed in preserved impact structures where crater rims are considered as catchment [7,16].

The second category includes the visualization of impact structures using multispectral satellite data, and derive the lithological discontinuities and structure features that might be associated with impact cratering [16,11]. Linear features derived from Landsat satellite data are used to define the orientation of linear geological structures and distribution of lithological units such as shock-induced alterations and ejecta of brecciated materials [16,20]. The radial and annular lineament patterns have been observed in several exposed impact structures as a result of concentric depressions and rim escarpments [15].

The third category is to automatically detect impact craters using automatic computer algorithms based on the circular morphometric similarities of impact crater structures visible in remote sensing data [21]. Several Crater Detection Algorithms (CDAs) have been conducted on extraterrestrial planets and moons such as Mars and Lunar craters [22,23]. However, limited attempts have been conducted to automatically detect terrestrial impact craters [24]. Masaitis et al.,[25] and Kenkmann et al.,[7] reported that complex geological processes and size variations of terrestrial impact craters could interfere the automatic detection of terrestrial impact craters. Li et al., [26] also highlighted a challenge to distinguish impact craters, volcanos, and valleys in deep learning for automatic crater detection because their resemblance characteristics which hinders optimal detection of the impact craters from remote sensing data.

The three types of impact crater including simple crater, complex crater, and impact crater basin (transitional), are characterized by different topographic features[2]. The simple impact craters are topographically indicated by sharp bowl-shaped depressions with a diameter of ~2 km for those occurred in sedimentary rocks and ~4 km for crystalline rocks [8,27]. The complex impact craters also recognized as circular or sub-circular topographic features with central uplift or concentric peak rings and a diameter greater than about 4 km. Moreover,

complex craters have a smaller depth to diameter ratio than simple craters [28,29]. The transitional craters have relatively flat floor with one or more discrete terraces, and the absence of sharp bowl-shaped topography and central uplift [29]. The terrestrial impact crater basins have a diameter ranging from 3 km – 10 km [7].

Previous studies have been focused on extra-terrestrial impact craters with limited studies on terrestrial impact craters. The purpose of this study is to provide a preliminary survey method for the identification of possible terrestrial impact craters from global digital elevation datasets. In view of geometric characteristics of impact craters, DEMs can quantify the geometric variables and therefore are the ideal data sources for reconnaissance investigation. For model development, this study collected 94 confirmed and well-preserved impact craters from worldwide areas. Then, based on object attributes a machine learning algorithm was tested for the classification of terrestrial impact craters from similar shaped topography and commonly found land features such as volcanic calderas and valleys. The most important variables for differentiating impact craters from other terrestrial topographic features are identified by the machine learning algorithm. We expect this approach could contribute to the discovery of new impact craters with well-preserved topography.

1.2. Materials and Methods

To figure out the optimal segmentation and detection of the exposed impact craters, the study investigated 94 (~ 45 % worldwide craters) confirmed exposed impact craters including 24 simples, 66 complex, and 4 transitional impact craters. The exposed impact craters are described as impact craters with a visible and distinct circular morphological expressions [7]. Furthermore, 104 volcanic calderas consisting of 44 single pit and 60 coalesced pits calderas distributed over the world have been used to test the detection performance of impact craters from similar topographic features (Figure 1, Table A2). The single-pit calderas are generally characterized by a single wide depression, while coalesced pits calderas are

characterized by multiple interconnected depressions within wider area [30,31]. The study incorporated volcanic calderas for machine learning object-based classification because they have been reported as the most analogous morphological features with those of impact structures in remote sensing data [11,32].

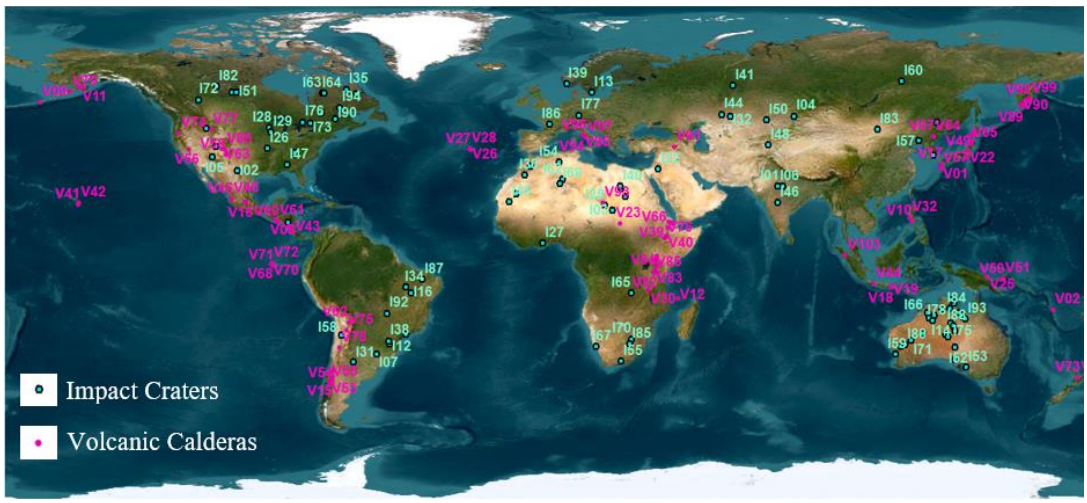

Figure 1. The sample of impact craters and volcanic calderas used in this study.

1.2.1. Data Acquisition and Preparation

This study used the worldwide Digital Elevation Model of Shuttle Radar Topography Mission data (SRTM DEM) for exposed impact craters and selected volcanic calderas with similar size of impact craters. The DEM data acquired on 23rd September 2014 with a resolution of 1 arcsec (~30 m/pixel) were downloaded from USA Geological Survey (USGS) [33]. 94 confirmed craters have been used in this study because of limitation of exposure and limited data coverage of SRTM data. The buried, submerged craters, and craters located in high latitude outside of SRTM view have not been considered [7] (Table A1). The buried and submerged impact craters are characterized by a lack of circular morphological expression on the earth's surface because of post impact geological processes such as weathering and erosion, and water bodies [2]. Additionally, 104 volcanic calderas with diameter sizes analogous to those of impact craters were chosen from Collapse Caldera Worldwide Database to test detection models [34] (Figure 1, Figure A2). Moreover, 124 valley objects that are mostly found in

mountainous and associated with various landscapes areas have been randomly selected during the segmentation process. They have been used as additional class for object-oriented classification to evaluate the detection performance of impact craters.

The original SRTM DEMs were filled to remove void pixels, and then the impact craters, and volcanic calderas were clipped to generate a single mosaic image including all target impact craters and other types of topographic features Figure 2. The extent of the clipped area was approximately 3 times the apparent diameter size of target impact craters or calderas. Then, additional morphometric layers including slope, aspect, and hillshade layers were derived from the DEM mosaic for object-oriented segmentation, following the findings from previous studies. These derivatives could enhance the circular topographic imprint of the rims that create a topographic contrast compared to the surrounding areas [21]. The four morphometric layers integrated eCognition developer 10.1 during the segmentation are illustrated for representative impact crater and volcanic caldera sections Figure A1.

1.2.2. Optimum Scale Parameter Selection for Impact Crater Detection

In Shuttle Radar Topography Mission data, each crater consists of many 30-m pixels that define its geometries and topography. Thus, to clearly define the boundary of impact crater, each crater should be extracted as an object. This study multi-resolution segmentation (MRS) was conducted in eCognition developer 10.1 for segmentation of the objects [35]. MRS involves a bottom-up region merging process of pixels. The segmentation starts by considering every pixel as a single object, and accumulatively merging homogeneous pixels into distinct objects based on the scale parameter, compactness, shape, texture, and color. The merging process gets stopped when the increase of homogeneity pixels exceeds the user defined scale parameter in eCognition software [21,36,37,38].

The size of segmented objected are mainly controlled by the user defined Scale Parameter (SP), and associated shape and compactness [39], and, thus, different scale parameters provide in different sizes of segments. To determine the best scale parameters for

optimal segmentation, the segmentation was iteratively executed with changes in scale parameters from 5000 to 60, thanks to the size variability of impact craters and calderas (Figure 2). In this study, the shape of 0.4 and compactness of 0.6 have been kept constant and used for segmentation because they detected the circular rims effectively based on trial-and-error.

The circumference of impact craters is topographically identified by the raised edge of the crater rim [7]. Based on this observation, we then hypothesized that the circular topographic imprint of the raised rim on the digital elevation model raster would cause the formation of homogeneous circular objects. We afterward carried out two steps assessment approaches to evaluate the segmentation results. First, the segmentation results at every SP were visually inspected to decide if the segmentation outlined the impact crater rims properly. Then, the segmentation results that passed the visual inspection were additionally evaluated with Area Fit Index (AFI). Area Fit Index (AFI) (equation 1) quantifies the fitness area between the reference area of impact craters (R) calculated from the Earth Impact Crater Database [2], and the area of impact crater object (S) derived from the segmentation.

$$AFI = \frac{area(R) - area(S)}{area(R)} \quad (1)$$

An AFI equal to 0 is an ideal segmentation and AFI values ≤ 0.5 are considered as a good agreement [40,41,42,43]. The number of adequately segmented impact craters and AFI have been summarized for every SP, and the SPs with the most impact crater segmentation and the minimum AFI have been selected as optimum scale parameters. The morphometric characteristics of impact craters segmented at each SP were analyzed to figure out the relationship between SPs and morphometric parameters.

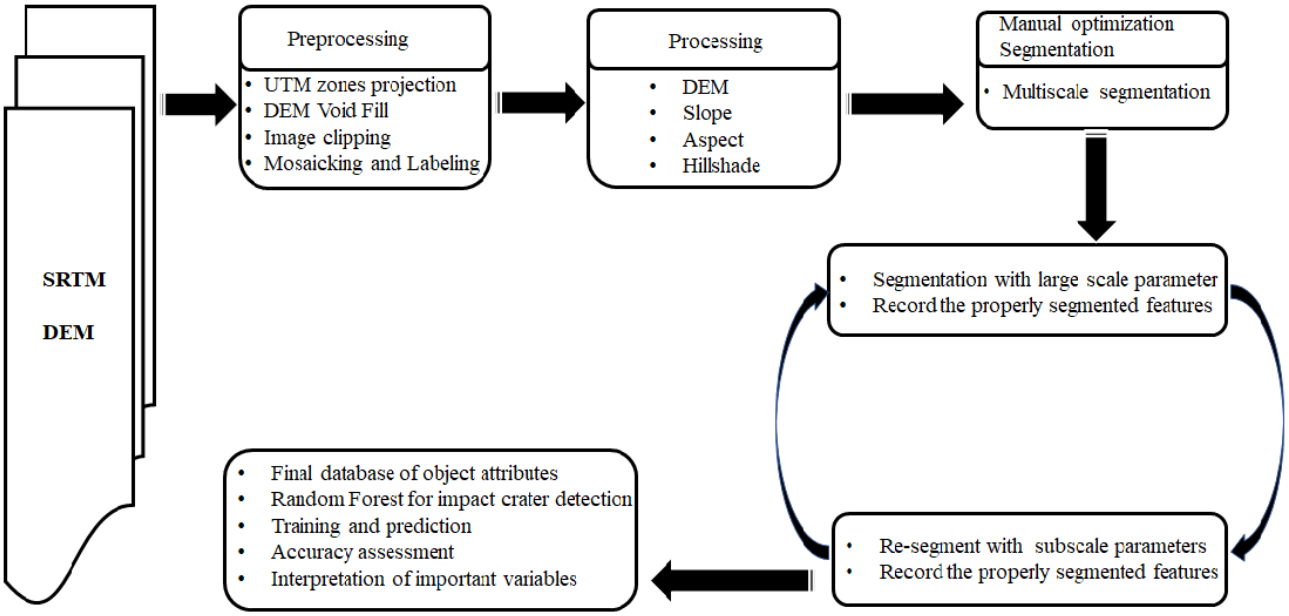

Figure 2. The workflow of multiresolution segmentation and object-oriented terrestrial impact detection

1.2.3. Random Forest Model for Terrestrial Impact Crater Detection

The objects segmented at optimal SPs for terrestrial impact craters were further used for the object-oriented classification model. Consequently, the objected attributes of segmented 70 objects of craters, 85 objects of calderas, and 124 objects of valleys have been used to generate a random forest-based detection model (RF hereafter). An overall of 16 attributes were derived from segmented objects and used for the RF classification model (Table 1). Among the 16 attributes, 7 topographic attributes expressed the morphological variation of the landform, 3 geometric attributes described the shape, and 6 texture attributes quantified the surface structure or pattern based on Gray–Level Co-occurrence Matrix (GLCM) (Table 1). For the sake of overfitting, multicollinearity analysis among the 16 variables was conducted. Based on the analysis, 5 variables with high intercorrelation were removed including Angular Second Moment (ASM), entropy, contrast, standard deviation of elevation and aspect, and 11 variables with low intercorrelation coefficient (< 0.6) have been used for the Random Forest classification model.

RF is a nonparametric machine learning algorithm based on randomly generated tree classifiers, and the classification is driven by the majority votes. In addition, important variables that effectively describes the relationship between predictors and target features can

be quantitatively derived by Mean Decrease Gini (MDG), and Mean Decrease Accuracy (MDA) scores [44]. Then, in this study the algorithm for classifying objects attributes was implemented in the R software based on eleven variables of detected objects. The bootstrap techniques have been applied to randomly split the entire data into datasets, and number of seeds was set to 300. 70 % of the samples were randomly selected for the training and 30% of samples for validation, and Ntrees and Mtry are 500 and 3, respectively (Figure 3). The variable importance of impact crater detection was rated based on Mean Decrease Accuracy (MDA) and Mean Decrease Gini (MDG) scores to figure out the major contributor of morphometric parameters for impact crater detection. The roles of major contributors have been discussed on how those variables could be used for terrestrial impact crater detection.

Table 1. The objects attributes extracted from detected objects.

Type	Parameters	Brief description	References
Topographic	Elevation	Express the height of an object below or above sea level	[45]
	Slope	Express the steepness of the surface of an object	[46]
	Aspect	Express the orientation of slope of an object	[47]
	Hillshade	Illustrate the impression of the 3D surface of an object from the point of view of the sun	[47]
	Standard deviation of elevation	Express the variability of elevation within the object	[48]
	Standard deviation of slope	Express the variability of slope within the object	[48]
	Terrain Relief	Represent the difference between maximum and minimum elevation within the object.	[49]
Geometric	Length/Width ratio	Represent the relative comparison between the length and width of an object	[45]
	Elliptical fit	Shape descriptor quantifies how much an area of an object fits the shape of an ellipse with a similar area.	[45]
	Circularity	Shape descriptor that quantifies the roundness of an object: $(Perimeter^2) / (4\pi * Area)$	[50]
Texture (GLCM)	Homogeneity	Estimate the similarity between the pairs of pixels in the image object.	[51]
	Dissimilarity	Estimate the difference between the pairs of pixels in the image object	

Angular Second Moment (ASM)	Estimate the amount of homogeneity or uniformity within the image object.
Contrast	Measure the local intensity variation in the image object
Correlation	Measure the linear dependency between the pairs of pixel values in the image object
Entropy	Measure the unpredictability or randomness of the relationship between the pixels in the image object

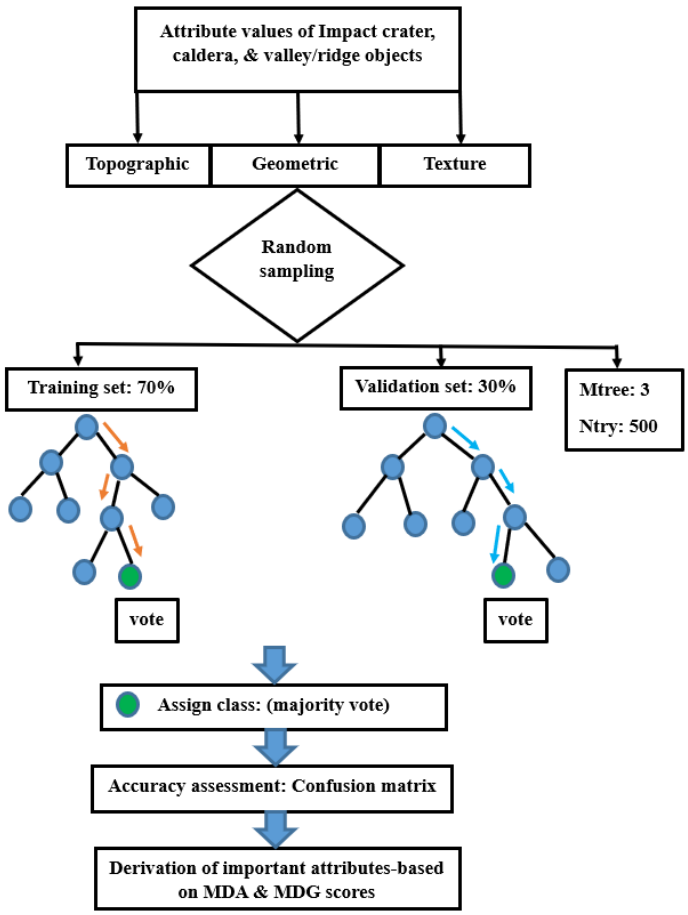

Figure 3. Random Forest model developed and identified important object attributes for impact crater detection.

1.3. Results and Discussion

1.3.1. Selection of Optimal Scale Parameter (SP) for Impact Crater Segmentation

The visual inspection of multi scale segmentation results from 5000 to 60 has found that the scale parameters and diameters of segmented impact craters have positive relationships where the crater rims for larger impact craters were properly segmented or outlined for larger SPs. Moreover, we found that SPs larger than 2000 would segment impact craters with approximately diameter ≥ 70 km, and SPs ≤ 2000 would segment impact craters with a diameter < 70 km.

The multiresolution segmentation process at various scale parameters from 2000 to 5000 have properly segmented only one impact crater from 5 impact craters in 70 – 180 km diameter range (Table 2). The properly segmented impact crater was Manicouagan impact crater (Canada) with a visible ring of ~70 km diameter at scale parameter of 3000. The SP 3000 effectively segmented the possible rim or ring whereas SP 5000 and 4000 under-segmented and 2000 over-segmented the outer rims (Figure 4a). In addition, an AFI value of 0.45 for the SP 3000 confirmed the good performance of segmentation. The rim of some craters such as Vredefort crater in South Africa had experienced erosion, causing the rim boundaries to become less distinct. Consequently, the segmentation process was unable to detect the evident rim boundary in such cases (Figure 4b). Large craters with diameter greater than 70 km are rare on the earth surface, which account for only about 5% of the samples. It might be attributed to Earth's atmosphere, geological activities, erosion, and plate tectonic compared to the other planets and the Moon [2, 52]. Therefore, we recommend SP3000 as the optimal segmentation parameter for craters larger than 70 km.

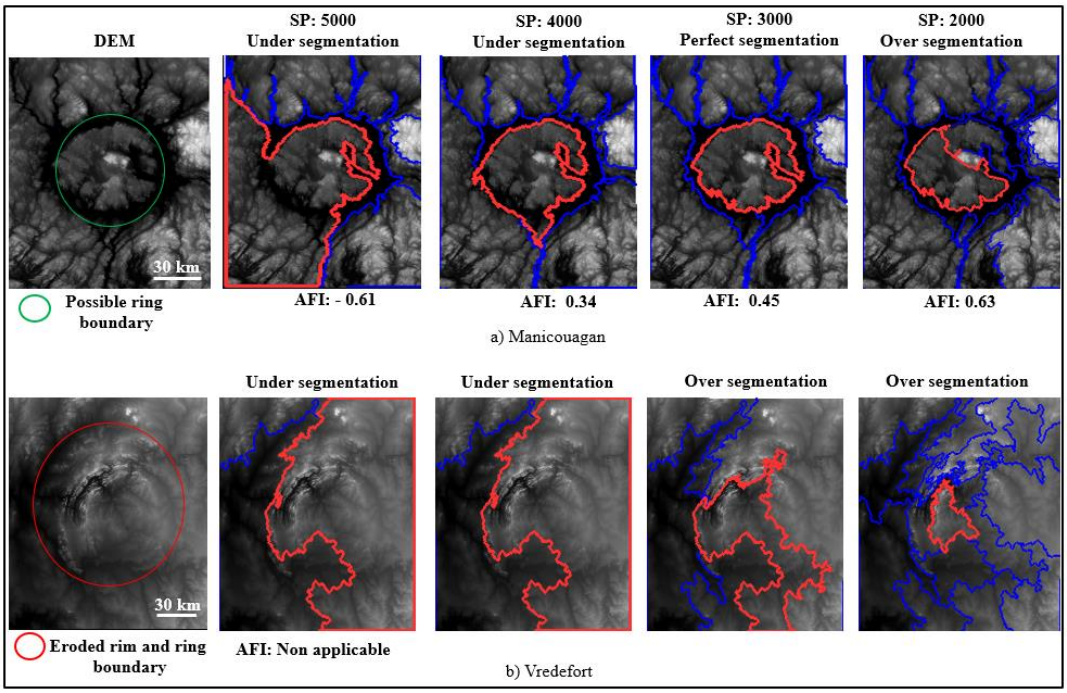

Figure 4. Multi resolution segmentation results for largest impact craters (a) Manicouagan impact crater (Canada); and (b) Vredefort crater (South Africa).

Similarly, the segmentation results of the other SPs (2000, 1000, 700, 400, 200, 100, 80, 60) were evaluated and the impact craters segmented from each SP varied depending on mainly the size in diameters and exposure level (Table 2, Figure 5). As a result, all SPs less or equal to 2000 except 60 have been selected as optimal scale parameters for impact crater segmentation. Moreover, a relatively high correlation (R^2) of 0.78 was found between the diameter of segmented impact and 8 SPs (Figure 5, Figure 6).

The SP that segmented the most impact craters was 200 and properly segmented 21 out 27 exposed impact craters in apparent diameter range from 1.8 – 12 km. The representative impact craters segmented by SP 200 is Goat Paddock crater (Australia) of 5 km diameter (Figure 5). The highest detected impact craters found in this scale has been simply related with the large population of terrestrial impact craters available in the diameter size range of 1.8 – 12 km. Indeed, a previous study has reported that almost half of terrestrial impact craters have a diameter range from 1 km to 10 km [7]. The smallest SP for impact crater segmentation found in this study was SP 80 which properly segmented 7 small sizes of impact craters out of 8 with diameter size in the range of 0.88 – 3.4 km. Then the smallest and well-preserved simple craters

including Tenoumer (Mauritania), Roter Kamm craters (Namibia), and Tswaing (South Africa) have been detected at the scale of 80.

Contrary to the other scale parameters, the SP 60 over-segmented all 10 small impact craters of 0.024 – 0.64 km diameter. These small impact craters provided indiscernible topographic imprints from neighboring features on satellite data of 30 m resolution (Figure A3) thereby providing indiscernible segmentation results. Hence, based on visual inspection the SP 60 has not been considered as an optimal SP because it provides unreliable segmentation results for impact crater detection.

Table 2. Attempted optimum scale parameters and number of detected features.

Segmentation settings			Impact craters			
SP	Shape	Compactness	Diameter range (km)	Count Segmented (%)	AFI	Count Not Segmented (%)
5000–3000	0.4	0.6	70 – 180	1 (1.0)	0.48	2 (2.1)
2000	0.4	0.6	24 – 60	8 (8.5)	0.07 – 0.50	0
1000	0.4	0.6	8 – 39	12 (12.7)	0.01 – 0.41	0
700	0.4	0.6	6 – 30	6 (6.3)	0.08–0.43	2 (2.1)
400	0.4	0.6	6 – 17	9 (9.5)	0.04 – 0.43	3 (3.1)
200	0.4	0.6	1.8 – 12	21 (22.3)	0.08 – 0.49	6 (6.3)
100	0.4	0.6	1.8 – 6	6 (6.3)	0.12 – 0.44	0
80	0.4	0.6	0.88 – 3.4	7 (7.4)	0.12 – 0.35	1
60	0.4	0.6	0.024 – 0.64	0	0	10 (11.7)
Overall:			70/94 (74.5 %)			24(25.5 %)

In general, a large overlap in segmented impact craters have been observed between the neighboring SPs (Figure 6). As a result of visual inspection, 8/11 SPs (3000, 2000, 1000, 700, 400, 200, 100, 80) provided the optimum homogeneous circular objects outlining the rim of 70/94 (74.5%) impact craters. The most well-preserved craters like Rotter Kamm (Namibia) and Vargeão Dome (Brazil) showed homogeneous circular segments with nearly zero AFI about 0.06 and 0.04 (Figure 5). However, the area of fit index showed a relatively high

goodness of fit for moderately eroded impact craters such as Charlevoix (Canada) and Ries (Germany) with AFI 0.5 and 0.45 respectively (Figure 5). On the other hand, 24/94 (25.5%) impact craters have not been properly segmented due to the lack of visible and detectable circular topographic imprints regardless of diameter. The impact craters rims like those of Rochechouart crater (23 km, France) and Kelly West (6.6 km, Australia) have been completely erased from the Earth's surface as result of post impact geological activities and are belonged to this group.

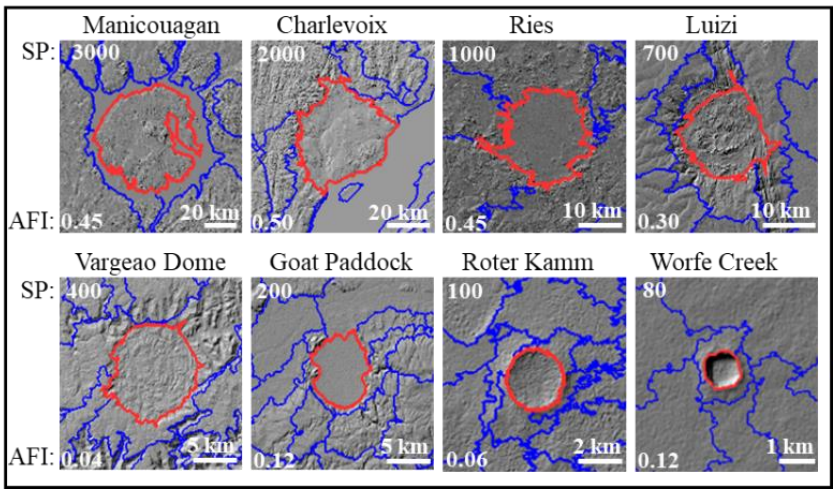

Figure 5. Multiresolution segmentation results of representative impact craters at different optimum scale parameters.

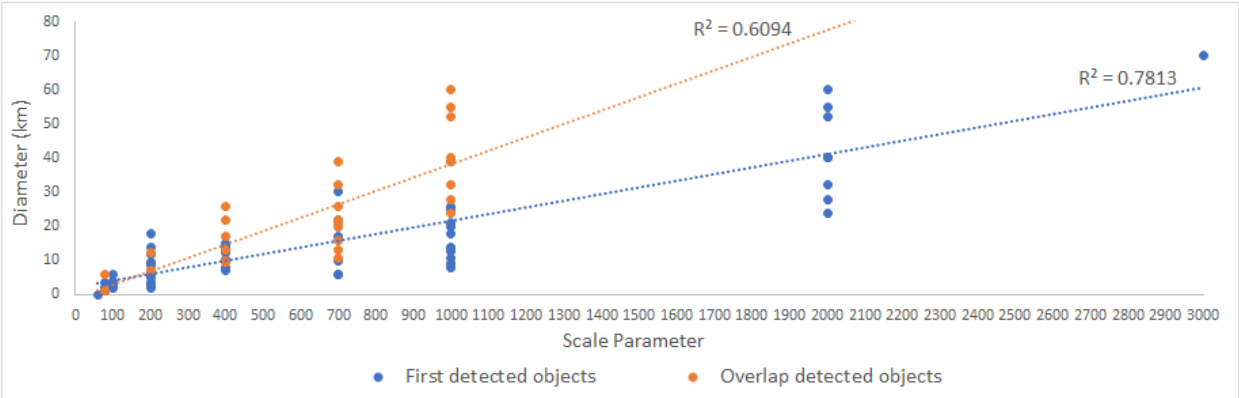

Figure 6. The overlapping situation for each scale impact craters.

1.3.2. RF Classification of Terrestrial Impact Craters and other Topographic Features

The terrestrial impact craters segmented from optimal SPs were compared with other segmented similar topographic features such as volcanic calderas and commonly found

topographic features like valleys based on the RF model. Similarly, the segmentation has been also performed for those topographic features. Consequently, a total of 85 volcanic calderas and 124 valleys' objects properly segmented were used for RF object-oriented classification. The object attributes explained in (Table 1) of terrestrial impact craters and other topographic features were then extracted and served as input variables in RF classification. 70 % of objects attributes (70 impact craters, 85 volcanic calderas, and 124 valleys) were applied for the calibration model and the rest 30 % were used for validation. The accuracy assessment showed the effectiveness of the classification model with very good overall accuracy of 88.4% and a kappa coefficient of 0.82. Notably, the model separated impact craters and calderas from valleys' objects very effectively with an accuracy close to 100% (Table 3).

Table 3. Confusion matrix of training, validation data from RF algorithm, where Production's Accuracy (PA) and User's Accuracy (UA) for each class are also presented.

TRAINING DATA					
Classes:	**Crater**	**Caldera**	**Valley**		
Crater	43	0	0	Accuracy	100%
Caldera	0	59	0	Kappa Coefficient	1
Valley	0	0	82		
VALIDATION DATA					
Classes:	**Crater**	**Caldera**	**Valley**	**PA (%)**	**UA (%)**
Crater	20	3	1	74.1	83.3
Caldera	7	23	0	88.5	76.6
Valley	0	0	41	97.6	100
OVERALL ACCURACY					
Accuracy				88.4	
Kappa coefficient				0.82	

However, the accuracy for detection of impact craters and volcanic calderas was relatively lower with an accuracy of 74.1 % and 88.5 % because they have similar topographic characteristics. Although the accuracy was the lowest for terrestrial impact craters, the accuracy of 78.7% is still considered good prediction accuracy. We therefore infer that the remote sensing approaches to preliminary detection of undiscovered terrestrial impact craters based on objects attributes can be effectively applied.

The important variables for the detection of terrestrial impact craters from other similar features were further deduced from Mean Decrease Accuracy (MDA), and Mean Decrease Gini (MDG) indices (Figure6). Based on the slope change indicated by a sharp decrease in MDA and MDG, the seven important variables have been discovered: circularity, length width ratio, relief, slope, elevation, homogeneity texture, and standard deviation of slope (Figure 7). In addition, the violin plots visualized the distribution of the 7 important variables of the three feature types based on the kernel density estimation (Figure 8).

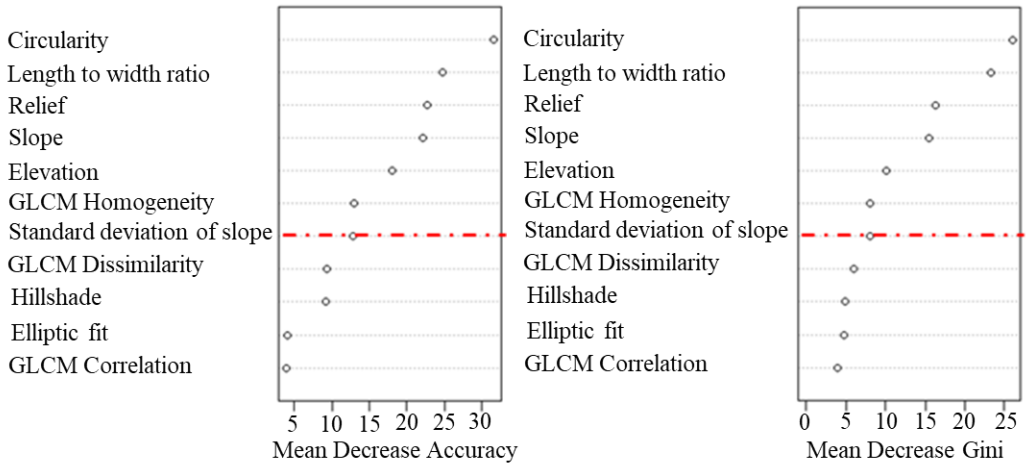

Figure 7. The ranking of MDA and Gini indices of importance variables, the 7 variables above the red dotted line indicated major role in impact crater detection.

The median locations, the shape and size of the violin plots presented a significant difference between the classes. The white dot points indicate the median of the data distribution along with the interquartile range, and the bulges in shape indicate higher probability density. Among the three attribute groups, it has been concluded that geometric attributes play the most important role in the detection of terrestrial impact craters, which is followed by topographic and surface texture attributes (Figures 6 and 7).

Circularity, a geometric attribute, was ranked as the most effective attribute for impact crater detection. Although both impact craters and volcanic calderas have circular shapes, they have differences in the statistical distribution. 75% of impact craters have circularity lower than 0.29 while 75% of volcanic calderas showed circularity higher than 0.22. A slight overlap was found in the range of 0.22 – 0.29 (Figure 8a). Meanwhile, valleys have distinctively lower circularity (Figure 8a). The circular shape of objects was further quantified by length to width

ratio. Half of the impact crater objects had a ratio higher than 1.5 and the majority of volcanic calderas (75 %) were lower than 1.6. More than 75% of valleys showed a high ratio (> 2.5) (Figure 8b).

In general, the difference between impact craters, volcanic calderas and valleys in terms of segment formation is mainly controlled by their formation, post impact and eruption processes. The impact craters displayed jagged object boundary, with relatively lower circularity, and higher length to width ratio compared to volcanic calderas. The angle of impact significantly influence the shape of craters where high angle impact produces higher circular craters than those of low angle impacts (oblique impactors) [7]. Indeed, prior studies have reported that 34 impact craters have elliptical form with long diameter axis to short diameter axis ratio above 1.05 [7]. The heterogeneity in target lithology played a major role in roughing the circularity of impact craters due to uneven stress distribution and rebound materials processes. Moreover, uneven erosion, and post impact deformation have been further contributed to elliptical formation and modifications of the circular form of terrestrial impact crater rims [7]. The crater rims are composed of ejecta, melted, and brecciated materials, and, thus, they are relatively vulnerable to erosion compared to crystalline igneous rocks. This phenomenon can also be confirmed by the ages of impact craters which is related to exposed time for erosion and post impact sedimentation in the central depression [53]. Indeed, the impact crater objects with higher circularity (>0.72) were observed for 5 preserved simple impact craters including Rotter Kamm, Worfe Creek, meteor, Tenoumer, and Tswaing craters, which have ages less than 5 Myrs [5].

On the other side, the volcanic caldera rims have relatively higher circularity regardless of age because of the collapse of the magmatic chamber tend to occur symmetrically around the central event of ring faults, and the volcanic eruptions tend to release the pressure unformally in all directions. In addition, the caldera rims mainly formed by crystalline igneous and other extrusive igneous rocks like basalts, and rhyolite rocks which have higher resistance to erosion [54]. However, the circularity of the caldera rims can be also affected by characteristics of subsequent collapses. This study only used 104 volcanic calderas out of over 400 calderas worldwide [52,55]. Thus, a fully detailed understanding the factors related to modification factors of the caldera rim circularity needs more worldwide cases. Conversely,

the valleys are low long laying areas, with relatively flat bottoms that often display jagged sides. They formed mostly elongated and asymmetrical objects that were associated with low circularity and high length to width ratio.

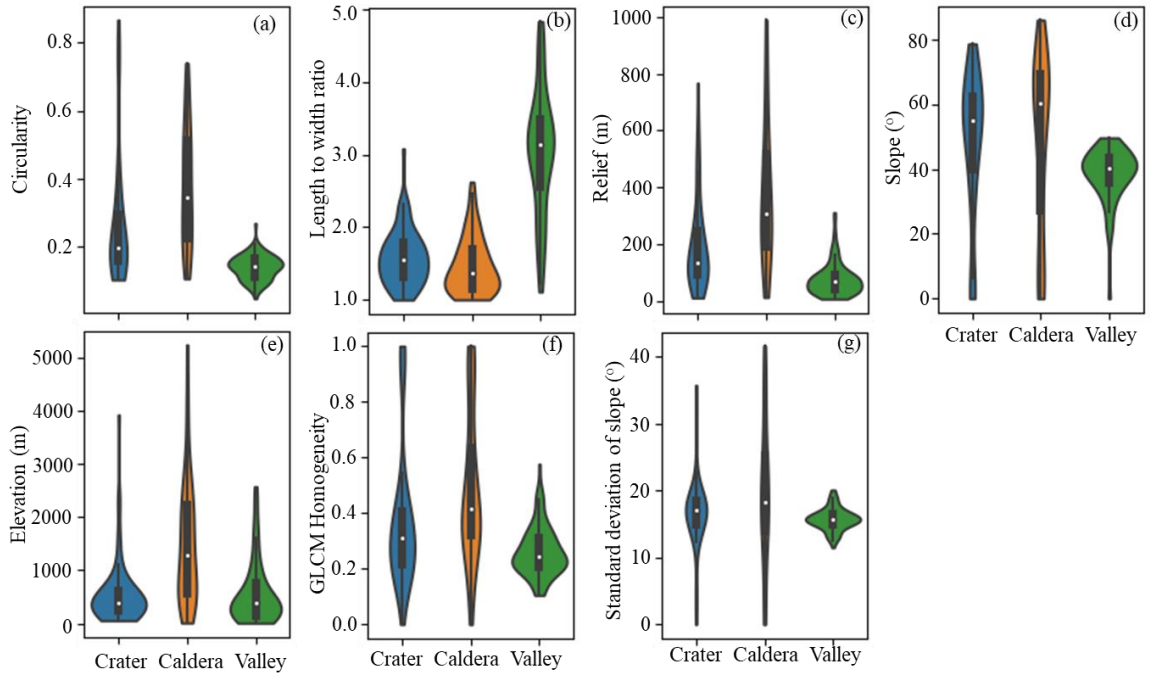

Figure 8. The illustration of the density distribution of seven major variables.

The topographic object attributes including relief, slope, and elevation have been found as reliable variables for discerning terrestrial impact craters based on segmented objects. The 75% of impact craters have been characterized by relief less than 245 m, whereas 75 % of volcanic calderas are higher than 192 m. The relief of valleys showed a wide overlap with impact craters where 95% were lower than 192 m because they share the similar topographic depression (Figure 8c). The relatively lower relief found for impact craters was associated with shallow topographic depression structures resulted from accumulative deposition of ejecta and post-impact sediment deposition [10]. The shallower depression of impact craters have been also observed for lunar craters which are characterized by a relatively lower depth to diameter ratio [56]. On the other side, the relatively high internal relief found for volcanic calderas could be associated with a deep central depression formed by the extensive collapse of the emptied magma chamber [57].

The slope attribute of impact crater objects showed that 75% of them were mostly characterized by relatively gentle slopes less than 62°. On the side the 50% of the volcanic calderas objects have been mainly indicated by very steep rims with slopes greater than 60.2°. Valley's objects have distinctively low slopes of less than 49.6° because they are generally characterized by low laying and relatively flat areas (Figure 8d). In addition, an important amount of impact crater objects (88.5%) was found in elevations lower than 1000 m, whereas the majority (60 %) of volcanic calderas are distributed in higher elevation ranges (1000 – 5233 m) (Figure 8e). The higher elevation mostly found for volcanic calderas can be justified by their relative topographic locations where most calderas are generally found in volcanic mountain summits that are relatively higher than most mountains.

The GLCM homogeneity was only one texture object attributes ranked as important variables, showed a significant overlap for all three features as well as standard deviation of slope (Figure 8f, g). A substantial proportion (75%) of impact craters and volcanic calderas showed a homogeneity of less than 0.4 and 0.63 respectively. Several impact craters showed a relatively low homogeneity compared to volcanic calderas and could be the result of surface roughness caused by fractured, brecciated materials and central multi-structure rings [58]. Moreover, 75% of valleys were also characterized by homogeneity lower than 0.31 (Figure 8f). Similar patterns are also observed for the standard deviation of the slope variable while volcanic calderas may have relatively higher variations in slope (Figure 8g).

1.4. Conclusion

This study introduced optimal scale parameters for segmentation of terrestrial impact craters, and object-oriented classification method based on confirmed and exposed terrestrial impact craters and DEM data. It found that conducting segmentation on remote sensing data like global digital elevation models can be effectively used in preliminary identification of terrestrial craters. This approach can be applied in undiscovered remote area locations as a reconnaissance survey. Furthermore, this study not only tried to detect terrestrial impact craters but also detected volcanic calderas and tested the separability of other morphological features such as valleys from the impact craters. However, the reliable application of this study was found craters larger than 0.8 km diameter. Then, in case the smaller craters need to be detected, high resolution DEMs are required such as the TanDEM-X DEM by the German Aerospace

Center. Furthermore, this approach can serve to screen down possible candidates of terrestrial impact craters where topographic morphological expression are still well-preserved on Earth's surface. More systematic geological analysis must follow up to validate the existence of terrestrial impact craters.

The optimal scale parameters have been introduced for the optimum segmentation of terrestrial impact craters, and other terrestrial topographic features based on four integrated morphometric layers. The multiresolution segmentation algorithm detected the circular topographic imprints of impact craters, and volcanic caldera rims from 4 morphometric layers derived from SRTM DEM data including elevation, slope, aspect, and hillshade. Then, eight scale parameters ranging from 80 to 3000 have been found as the optimum scale parameters for terrestrial impact craters detection based on visual inspection and goodness of fit area of segmented impact crater objects. The optimum SPs indicated the goodness of fit area objects (0.01 – 0.5) and high correlation (R^2=0.78) with rim diameter within 0.88 – 100 km diameter range. Given the fact that terrestrial impact craters with wide diameters (>100 km) are rarely found (<5 %) because of high atmospheric pressure [52], SP of 3000 could be the optimal segmentation parameter for large terrestrial impact craters. The smallest impact craters (0.024 – 0.64 km) showed unreliable results and have indiscernible topographic imprints in 30 m resolution satellite data because they are subjected to the surface erosion and other post geological activities that resurface the Earth's crust[11]. Therefore, the segmentation scale parameter threshold for terrestrial impact craters with SRTM DEM is 80, which segmented impact craters of 0.88 km in diameter, and was considered as minimum scale parameter in this study.

The object-oriented classification using Random Forest successfully detected terrestrial impact craters as well as volcanic calderas and valleys showing overall accuracy of 88.4% and a Kappa coefficient of 0.8. The lowest detection efficiency 78.7% was found for impact craters as result of misclassification with volcanic caldera objects as they share the similar morphological features. The highest detection efficiency was found for valleys objects (98.8%) followed by volcanic calderas (82.6%). The highest detection observed for the valleys objects could be associated with a noticeable difference in elongated shape of valleys compared to the circular objects of impact craters and volcanic calderas. Although the detection accuracy

was lowest for terrestrial impact craters, but still acceptable and considered as good prediction accuracy. Thus, it infers that conducting multiresolution segmentation approaches on remote sensing global digital elevation datasets to the preliminary detection of undiscovered terrestrial impact craters can provide a reliable result.

The important variables for the detection of terrestrial impact craters were identified where the geometric played the most role followed by geometric and texture variables. The circularity, length to width ratio, relief, slope, and elevation indicated a major difference in medians while GLCM homogeneity and standard deviation of elevation indicated a minor difference in medians of violin plots. The terrestrial impact craters, in general, have been indicated by relatively lower circularity and higher length to width ratio compared to volcanic calderas, and significantly higher circularity and lower length to lower ratio compared to valleys. Moreover, the terrestrial impact craters have relatively lower relief, slope, and elevation than volcanic calderas and significantly higher relief, slope, and elevation than valleys. These geometric and topographic differences could be interpreted by the formation and geological processes of impact crater and volcanic caldera features. Impact craters are formed by celestial bodies impact with planets or moon's surface inducing the central depression, accompanied by deformation and brecciation and fall back of ejected materials. All those processes reshape the final structure of impact craters compared to the surrounding areas. The final structure of the impact craters such as crater rims or central uplifts are therefore mainly composed of brecciated, melted materials as result of impact energy and shock waves.

On the other side, the volcanic calderas are formed by volcanic eruptions, and sinking of collapse magmatic chamber, mostly symmetrical, resulting crystalline, and basaltic volcanic walls with deep central depression. This geological process and formation of impact craters make them more susceptible to surface erosion, weathering, and modification of final structures. It infers that the apparent rims of impact craters would lose circularity and topographic variations by lowering rims and filling central depressions over time. In addition, the impact craters have lower elevations than volcanic calderas, because the volcanic calderas are located at the top of volcanic mountains mostly forming higher mountains[59]. Moreover, the GLCM homogeneity of elevation could be included as a useful variable as brecciated materials mostly

found for impact craters could induced a relative rough texture compared to the crystalline and igneous basalts rock mostly form volcanic calderas.

Considering that the study used a wide range of exposed and confirmed terrestrial impact craters 94 (45 %) with diameter size ranging from 0.88 to 100 km, the method can be generally applied to the detection of unidentified craters worldwide using the global DEM models as a reconnaissance survey method. In addition, as the study included the similar features, such as volcanic calderas and valleys in testing the detection of impact craters, this approach could be used to screen down the impact crater candidates from the similar features.

Therefore, the segmentation parameters and detection variables introduced in this study would significantly contribute to the discovery of hidden terrestrial impact crater candidates in developing countries and remote areas.

CHAPTER 2. DEFINING IMPACT CRATER TYPES BASED ON TOPOGRAPHIC PROFILES.

2.1. Introduction

The geological process and bowl-shaped morphology of Jeokjung Chogye Basin (JCB hereafter) have attracted impact crater scientists community in the Korean Peninsula. The surface morphological expression of JCB is characterized by a concave depression with around 7 km rim diameter located at 128.261°E, 35.541°N, in South Korea (Figure 9). The JCB is indicated by upraised ring ridge of crater rim with a narrow breach in north eastern part [60]. The hydrology catchment of the crater basin is mainly fed by two main rivers, the Hwang river in the Western and Nakdong river in the Eastern part of the basin. The geological studies revealed that the target lithology of JCB crater is the cretaceous sedimentary rocks in Gyeongsang Basin. Gyeongsang Basin is mostly formed by Jinju formation (shale, sandstones) and Chilgok formation (mudstones, shale, sandstones, and conglomerates) [60, 61]. Currently The JCB is dominated by anthropogenic activities such as residential and farming activities.

The impact crater research team of the Korea Institute of Geoscience and Mineral Resources (KIGAM) conducted integrated geological surveys and drilling operations and revealed the impact origin evidence from the drilled cores. The discoveries of ultimate impact crater evidence including megascale and macroscale evidence such as shatter cones and Planar

Deformation Features (PDFs) confirmed that the JCB formation was driven by the meteorite impact. In addition, the first attempt of dating JCB crater used radiocarbon dating based on charcoals extracted from the lacustrine sedimentary cores, found JCB as relatively young crater with age of 0.03 – 0.063 Ma [61]. Previous studies also analyzed geochemical characteristics of the JCB impact crater based on Highly Siderophile Elements (HSE) and Re-Os isotope studies but did not reveal unambiguously the impactor type [62]. They found the presence of meteorite components such as relatively high Platinum Group Elements (PGE) and lower $^{187}Os/^{188}Os$ ratios. On the other hand, the geophysical gravity data predicated the impactor direction, where the impactor was steeply inclined from east to west (50 – 60°) from the ground [60].

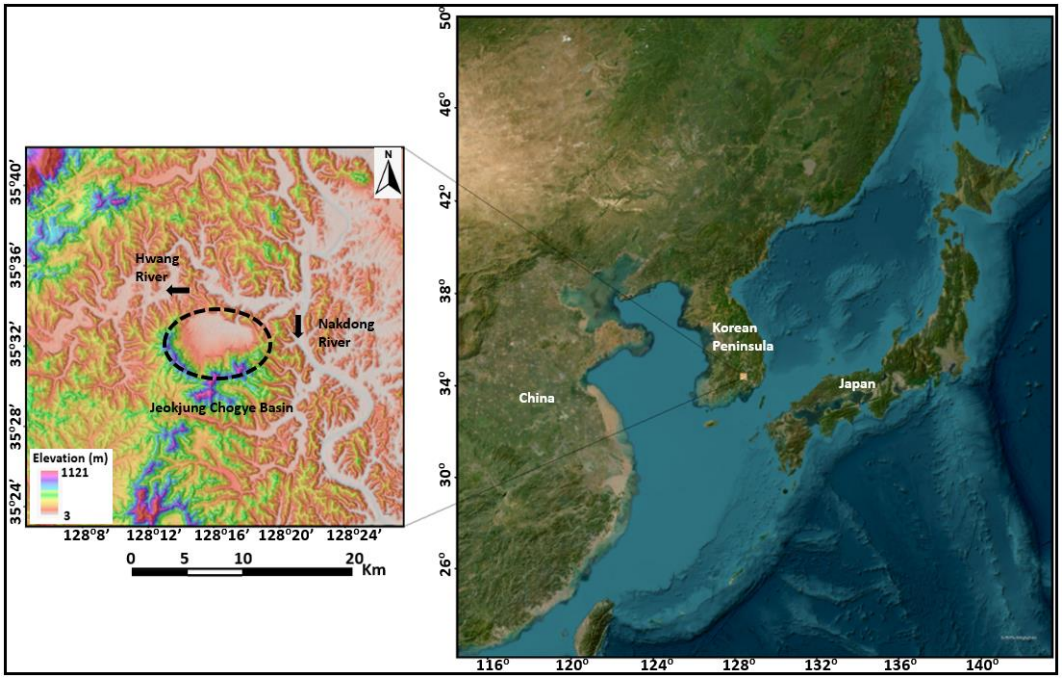

Figure 9. The illustration of Jeokjung Chogye Structure in terms of Digital Elevation model (DEM) displayed over the hillshade layer.

The JCB crater as the most recent discovered impact crater in southern east part of Korean Penesula, the previous studies have been first focused on conclusive evidences of impact craters, and estimation of impactor direction [60 – 62]. However, the previous studies did not put into priority the investigation of crater type associated with the morphology of JCB crater. The morphology of impact craters consists of simple, transition and complex craters. The physical properties of impactor like size, velocity, composition of the impactor, gravity of

the planetary body, and property of target lithology control the formation of different crater types[63]. The simple impact craters are originally characterized by sharp bowl-shaped topographic depressions, smooth inner walls, relatively high depth-to-diameter ratio, and slightly raised and overturned rims above the surrounding landscape. The diameter size of simple craters approximately range to 2 km for sedimentary rocks and 4 km for those formed in the crystalline [64]. Regarding to the complex impact craters, they are characterized by a circular shape with a relatively low depth-to-diameter ratio, central uplift peak rings, terraced walls, and sometimes breached rims [63, 65]. The transitional impact (impact basin) craters are indicated by flat floor, relatively small depth-to-diameter ratio, absence of sharp bow-shaped like simple carters, lack of central uplifts, and often terraced crater rims [29]. The size of transitional terrestrial impact craters ranged within the 3 to 10 km diameter size [7].

The Digital Elevation Models (DEMs) derived from mostly satellite remote sensing data have been used in numerous extraterrestrial and terrestrial impact craters to quantify the geometric characteristics [5, 56, 65 – 68]. The morphometric parameters measured from the topographical profiles such as apparent rim-to-rim diameter, crater floor diameter, central uplift diameter, depression depth, and terraced wall width, have been used to preliminary define the types of impact craters [7, 29, 69, 70]. The recent terrestrial impact crater database [7] includes 56 simple, 140 complex, and 7 transitional impact craters confirmed by systematic geological evidences and morphometric analysis. So far, the JCB impact cater has been validated as an impact crater by geological evidence while the morphometric analysis and definition of specific type is not clear.

This study aims to analyze and classify morphometric parameters of confirmed and well exposed terrestrial impact craters thereby suggesting the possible impact crater type of JCB. The topographic profiles of JCB impact craters were extracted from Shuttle Radar Topography Mission Digital Elevation Model (SRTM DEM) data and systematically analyzed the morphometric characteristics with regard to other 52 representative confirmed impact craters. Moreover, statistical analysis and machine learning classification have been applied to figure out the type of JCB impact crater based on morphometric parameters of 52 confirmed impact craters and the JCB impact cater. Finally, the major morphometric parameters contributing to defining the types of terrestrial impact craters are introduced.

2.2. Materials and Methods

2.2.1. Terrestrial Impact craters Database and exposure characteristics

To define the morphological characteristics of each type of impact crater and comparative analysis with JCB impact crater, this study used confirmed impact craters from terrestrial impact crater records [7]. It is the latest updated impact crater database with 198 confirmed craters and 10 possible craters. The database classified the impact craters into 60 simples, 141 complex, and 7 transitional (basin) craters, where 89 are found in sedimentary, 56 crystalline, and 63 mixed lithology. The database also divides the craters into 5 levels based on exposure status; 73 exposed, 40 partially buried, 44 visible circular morphology, 30 submerged, and 21 completely buried. However, some impact craters have multiple exposure characteristics, and, thus, the definition of exposure status is ambiguous.

To make a better exposure definition, we additionally included the exposure attributes from the encyclopedia atlas for terrestrial impact craters [2]. The encyclopedia explains the morphological exposure status as preserved, moderately eroded, deeply eroded, and buried for 185 craters due to morphological preservation level. Furthermore, the visibility of morphological expressions such as the rims and central uplifts is described in the database. The database consisted of 45 craters as clearly visible, 71 craters as poorly visible, and 69 craters are not visible. The clearly visible rim morphologies are dominated by well and moderately eroded craters, whereas the poorly visible and not visible morphologies are mostly found for deeply eroded and buried caters. The exposure status and morphological preservation characteristic of terrestrial impact craters are therefore summarized in Table 4 [2, 7, 29, 71, 72].

In addition, the modified database was further verified with other available continent-based databases [10, 73 – 76]. We finally concluded the exposure status of 14 well preserved, 58 moderately eroded, 66 deeply eroded, and 70 buried impact craters. The morphological type and exposure states are summarized in Table 5. The modified database has been then used to analyze morphometric characteristics for every type of impact crater. The morphometric analysis using global digital elevation model requires detectable surface features. Then, the deeply eroded and buried impact structures have been excluded from the analysis due to the lack of sufficient topographic expression on the surface. Since, it is an uncertain to recognize the small impact craters in 30 m SRTM DEMs, the impact craters with a diameter of

less than 0.8 km have been also excluded from this study. Moreover, the impact craters outside the SRTM coverage view at high latitudes have not been also considered.

As a result, 52 confirmed morphologically well-preserved and moderately eroded craters and JCB impact crater have been analyzed in this study (Table 5). The cumulative size frequency distribution (CSFD) of the selected impact craters with diameter ranging from 0.88 to 40 km, and age varied within 0.049 – 630 Ma is illustrated in Figure 10. where the JCB crater is represented by red mark. Among the 52 craters, simple, complex, and transitional craters comprised 11, 38, and 3, respectively where complex impact craters are dominated by moderately eroded and simple impact craters dominated by well preserved (Table 5).

Table 4. The morphological characteristics of different exposure levels [2, 7, 29, 71, 72].

Well preserved	Moderately eroded	Deeply eroded	Buried
• Distinct rim • A smooth raised rim boundary around the depression • A smooth bowl shape for simple craters • A nearly smooth central uplift ring for complex craters	• Jagged or fragmented rim structure • The absence of a raised rim boundary in some sections of the crater circumference • Altered bowl shape for simple craters. • Altered, submerged, or buried central uplift ring	• Absence of rim • The rim boundary nearly indiscernible in all sections • Altered and obscured bowl shapes for simple craters • No central uplift structure discernable	• Underground or submerged. • No exposed rim feature present at the surface • No topographic expression at the surface

The profile analysis, morphometric characterization, statistical test, and machine learning classification have been used for those impact craters and come up with the high possible crater type of JCB. However, transitional (basin) craters were only analyzed for profile analysis and morphometric characterization due to insufficient data.

Table 5. The statical summary of morphology and exposure status of the impact craters.

Impact Crater type	Exposure level							
	Well preserved		Moderately eroded		Deeply eroded	Buried	Total	
	Database	Our study	Database	Our study	Database	Database	Database	Our study
Simple	13	9	11	2	20	16	60	11
Complex	1	1	44	37	46	50	141	38
Transitional	0	0	3	3	0	4	7	3
Total	14	10	58	42	66	70	208	52

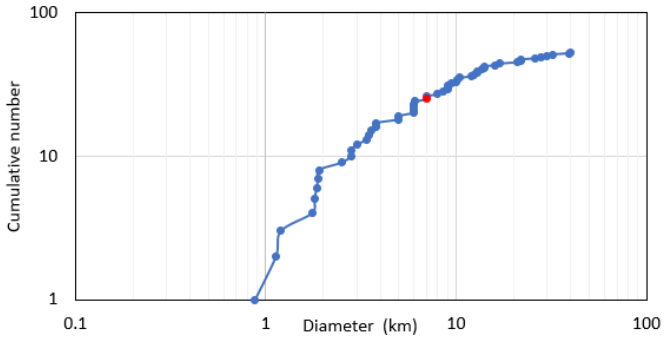

Figure 10. The cumulative size frequency density impact craters used in this study.

2.2.2. SRTM DEM raster images preparation and morphometric measurement

The SRTM DEMs for a total of 53 craters including the JCB crater were collected from USA Geological Survey (USGS) [33], for morphometric analysis. The SRTM DEMs with 1 arcsec (30 m/pixel) resolution of the JCB crater and 52 selected craters from the database were projected to their respective UTM zones and clipped for each impact crater. Then, 8 radial profiles were extracted for each impact crater with a radius two times larger than the rim diameter to cover the geologic context in the vicinity. For each profile, four morphometric parameters were measured including rim diameter (D), floor diameter (Df), depression depth (d), and width of crater wall (W) as illustrated in Figure 11. The rim diameter (D) infers the distance between the rim crests at opposite ends, depression depth (d) is the relief between the rim crest and crater floor, floor diameter (Df) represents the distance measured at the crater floor between the crater walls, and width of crater wall (W) is defined by D and Df in equation 2, respectively [77–79]. Finally, the standard deviation to express the measurement error of morphometric parameters was also calculated.

$$W = \frac{D-Df}{2} \quad (2)$$

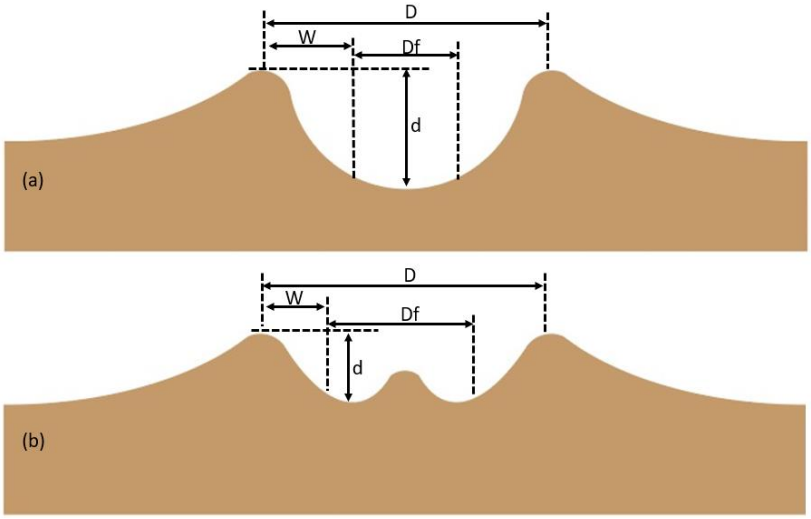

Figure 11. The ideal illustration of morphometric parameters (a) Simple and (b) Complex impact craters, adapted from [79].

2.2.3. Hypothesis Test Statistics and Random Forest Model

To figure out whether the morphometric parameters are statistically distinguishable between simple and complex crater types, the hypothesis test statistics was conducted. The normality test based on Kolmogorov Smirnov test [80] was first carried out to find the reliable hypothesis test for our data. Kolmogorov Smirnov test is preferred for the sample size greater than 50 and assume that sample data are normally distributed as the null hypothesis (H0). This study tested morphometric parameters (D, d, Df, and W) measured from eight profiles for each impact crater, namely 84 profiles for 11 well-preserved simple types and 304 profiles for 38 complex type craters using IBM SPSS Statistics 26 software. When the p-value of Kolmogorov-Smirnov test is less than the significance level (0.05), the null hypothesis is rejected, and concluded that the data is not normally distributed.

A non-parametric hypothesis test, Mann Whitney U test, is commonly preferred for the case that the data is not normally distributed [81]. Mann Whitney U test does not require any assumptions and investigates if there is a significant difference between two categories with regard to the central tendency of data distribution [82]. In this study, the null hypothesis assumed the distribution of the morphometric parameters is the same across both simple and complex types. Wherever the p values were less than a significant level (0.05), the null hypothesis was rejected suggesting that there is a significant difference in morphometric

parameters between simple and complex craters. Then, the morphometric parameters useful for distinguishing simple and complex craters were defined.

In addition, this study evaluated the statistical similarity of morphometric parameters of the JCB crater to simple and complex based on One Sample Wilcoxon Signed Test. One Sample Wilcoxon Signed Test compares the sample median and predefined specific value [83]. For both crater types, the null hypothesis (H0) assumed no difference between median parameters compared to JCB's median value, where the level of significance was less than 0.05, the alternative hypothesis was suggested.

The same morphometric parameters were afterward imported into a machine learning environment to develop the Random Forest (RF herewith) model. The RF is a non-parametric machine learning algorithm based on bootstrap technic and the majority of votes. It has also the advantage of recognizing variable importance and ranks the important variables that played the most significant role in the model's prediction based on Mean Decrease Accuracy (MDA), and Mean Decrease Gini (MDG) [44]. The RF is mainly controlled by Ntree and Mtry and were set to 142 and 2 respectively in R software. The 70 % of morphometric parameters were randomly selected from simple and complex impact craters to calibrate the model, and 30 % including JCB's morphometric parameters were used to test the model. The confusion matrix and important variables have been discussed on how JCB's morphometric parameters have been classified. In addition, important morphometric variables played a major role in separating simple and complex impact craters are defined.

2.3. Results and Discussion

2.3.1. Morphometric Characterization of Impact Craters and JCB crater

The topographic profiles have been used to measure the morphometric parameters, rim diameter (D) crater depth (d), floor diameter (Df), and crater wall width (W), for 53 selected impact craters including the JCB crater. In general, 9 simple well-preserved impact craters have a well-defined smooth concave shape surrounded by upraised rims, where the rims can be detected from all 8 profiles (Figure 12a). However, the distinct rims of the 2 moderately eroded simple craters were detected from six profiles out of 8 profiles because of erosion (Figure 12b). Thus, the sample numbers of measurable morphometric parameters of moderately eroded craters were relatively smaller than well-preserved ones. The profile of the complex well-

preserved crater is based on only one sample, Serra da Cangalha Crater, where the upraised rim and central uplift are well defined from all 8 profiles (Figure 12c). On the other hand, the 22 out of 38 moderately eroded complex impact craters did not show clear central uplifts due to the erosion or post impact geological processes (Figure 12d). Moreover, unsymmetrical profiles showing unbalanced rim height are detected from 4 to 6 out of 8 profiles in average (Figure 12d). The absence of central uplift and unbalanced rim height resulted from the post geological activities like erosion, weathering, and post sediment deposition [70]. Regarding the 3 impact craters belonging to the transitional type, 7 to 8 profiles showed a topographic depression with an upraised rim, where all profiles did not show any signature of the central uplift (Figure 12e).

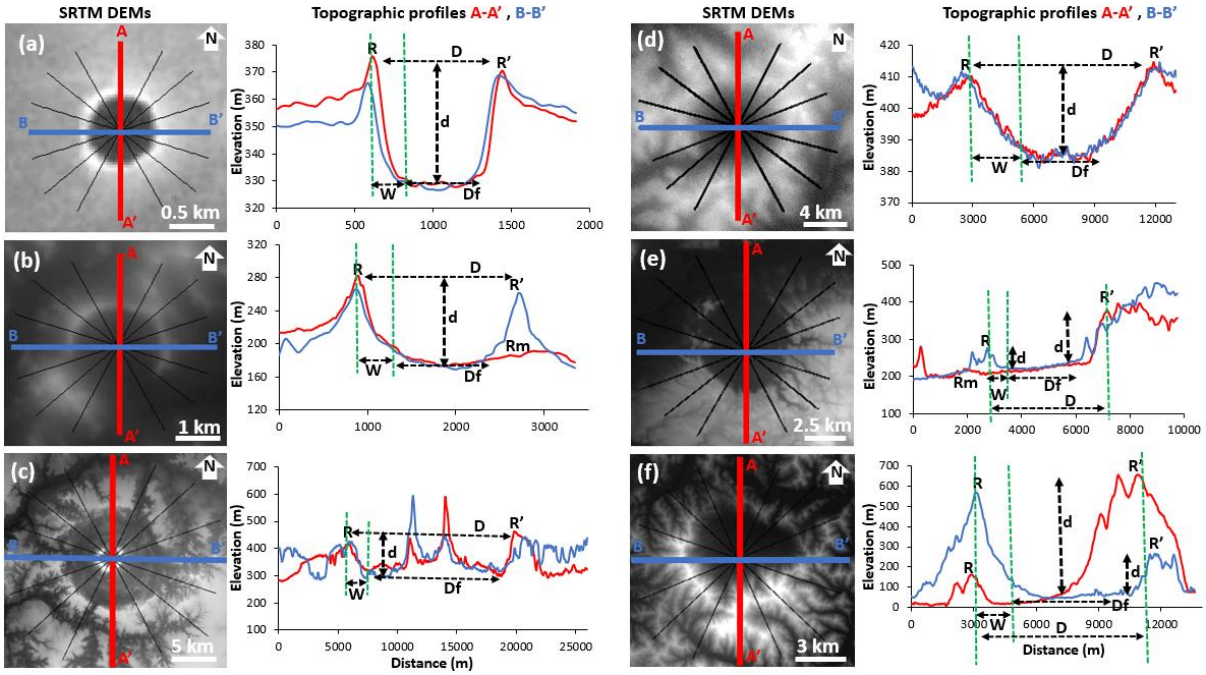

Figure 12. The representative topographic profiles for (a) preserved simple crater, Wolfe Creek, 0.8 km, Australia ; (b) moderately eroded simple crater, Yilan, 1.8 km, China; (c) preserved complex crater, Serra da Cangalha, 13.7 km, Brazil; (d) moderately eroded complex crater, Connolly Basin, 9 km, Australia ; (e) moderately eroded transitional craters, Goat Paddock, 5 km, Australia; (f) JCB crater, 7 km, S.Korea; and the associated morphometric parameters; **R-R':** rim diameter (D), **d**: crater depth, **Df**: floor diameter, **W**: crater wall width, and **Rm**: missing rim signature on profile.

The topographic pattern observed for eight profiles across the JCB crater displayed a concave shape, without any signature of the central uplift. Six profiles out of eight showed unsymmetrical circular depression with a pronounced upraised rim in the southern part

compared to the northern part of the crater (Figure 12f). Based on the pattern of topographic profiles, the JCB crater has a similar shape to either a simple moderately eroded type or a complex moderately eroded type.

The statistical morphometric parameters for 53 impact craters are summarized in Table 6. Considering the exposure status solely, all four parameters did not indicate a major difference between preserved and moderately eroded craters for the same crater types (Table 6). A minor difference between well preserved and moderately eroded was only observed for 2 moderately eroded simple craters that showed a relatively high standard deviation of D and W compared to the 9 well-preserved simple craters. The irregularities in circular rim structure caused by inconsistencies in mass wasting on the crater wall could be associated with relatively high standard deviation. In addition, uneven post impact geological processes such as erosion and weathering might also contribute to the irregularities in missing parts of the crater features. Although a direct comparison in standard deviation for complex type lacks statistical significance due to limited data for well-preserved type, previous researches reported that the post impact geological processes cause a substantial mass transport from crater wall and rim to crater floor affecting morphological parameters [84].

On the other side, the morphometric parameters show a significant difference despite minor overlaps based on the crater types. The simple impact craters have been characterized by smallest size in diameters, and wall widths followed by those of transitional and complex craters. In this study, the rim diameters measured across 11 simple craters ranged in (0.8 – 4.1 km), followed by 3 transitional craters ranged in (3 – 6.5 km), and showed an overlap with 38 complex craters ranged in (3 – 42 km).Nevertheless, the crater depth indicated a significant increase particularly in complex craters, but a major overlap was observed for across all crater types(Table 6). Table 6 indicated the statistical distribution of measured morphometric parameters at different crater types and their respective exposure levels. The simple impact and transitional craters showed a very shallow crater depths in 0.039 – 0.160 km, and 0.036 – 0.129 km respectively followed by complex crater with a prominent increase of crater depth (0.048 – 0.674 km). This observation is consistent with fresh lunar craters, where complex craters are deeper than simple and transitional craters regardless of the effect of degradation and post impact collapse [56, 84]. The floor diameter and wall width followed the same trend as the rim

diameter, their increases are generally related with the increase in rim size. The simple impact craters displayed a small floor diameter (0.19 – 2.5 km), followed by transition craters in (1.16 – 3.9 km) and complex craters (0.86 – 30 km). Additionally, the wall width shows a direct relationship with floor diameter, where the wall width decreases with an increase in the floor diameter as reported in previous studies (Table 6) [77, 78]. In general, all morphometric parameters showed a dramatic increase for complex craters compared to the simple and transitional craters.

The parameters measured from 8 profiles for JCB crater, they varied within 6.2 – 7.8 km for rim diameter, 0.12 – 0.62 km for crater depth, 3.9 – 5.3 km for floor diameter, and 1.3 – 2.05 km for wall width (Table 6). The parameter values are generally higher than those of 11 simple craters and lie mostly within a range of those of complex craters. Hence, considering these results, it is likely that the JCB crater may not be a simple crater despite of the absence of central uplift expressions on the Earth's surface. In addition to the asymmetrical profiles mentioned above (Figure 11f), the rim diameter of the JCB crater showed an elongation in the western to eastern direction that could be caused by oblique impact. Moreover, the aspect ratio estimated the ration between the maximum and minimum rim diameters 1.4 which deviate from perfect circular shape. Figure A4 illustrated the stacked eight profiles of JCB extracted from SRTM DEM, where the elevation in southern part of the rim is relatively more elevated than that of northern part. Indeed, [60] confirmed an oblique impact from the eastern direction based on gravity studies.

In addition, the box plots visualized the statistical distribution of morphometric parameters for various crater types (Figure 13). The rim diameter, floor diameter, and wall width indicated an evident difference with a minor overlap between the simple and complex impact craters. The morphometric parameters of JCB parameters remarkably coincide with those of complex craters rather than simple craters (Figure 13 a, c, d).

Table 6. The statistical summary of measured morphometric parameters, Min, Max, Av. and SD stand for minimum, maximum, average and standard deviation values respectively.

Parameters (Meter)	Simple								Complex								Transitional				JCB			
	Well preserved				Moderately eroded				Well preserved				Moderately eroded				Moderately eroded				Moderately eroded			
	Min	Max	Av.	SD	Min	Max	Av.	SD	Min	Max	Av.	SD	Min	Max	Av.	SD	Min	Max	Av.	SD	Min	Max	Av.	SD
D	839	2909	1758	30–167	1797	4189	3115	217–344	12825	14581	13999	597	3010	42308	13181	241–2396	3009	6506	4303	157–441	6254	7824	7230	498
d	39	160	92	2–30	57	156	102	18–26	63	127	91	24	48	674	106	2–77	36	129	82	12–17	120	620	330	186
Df	196	1833	792	27–214	976	2549	1870	131–150	10866	12446	11368	554	868	30015	8111	163–2138	1163	3924	2535	193–432	3940	5324	4737	472
W	177	820	483	29–114	253	1039	633	198–225	1531	2752	2087	283	241	11186	2535	92–1531	452	1398	884	179–224	1317	2052	1652	255

However, the quantitative distribution of crater depth displayed an overlapping across all crater types (Figure 13b), which indicates that the apparent crater depth is unable to distinguish various types of impact craters. An ambiguous difference in crater depth is mostly driven by rheological materials of target lithology and post geological modification processes that gradually and unevenly change the apparent depth over time [85]. As discussed for the preservation of impact craters, well-preserved impact craters are generally younger they have been mainly exposed to the weathering process for relatively shorter time than others. The crater depth gets shallower with exposure time because of the accumulative deposition of inward crater wall collapsed and weathered materials. Moreover, the material walls with weaker lithology to weathering likely experience even faster mass transport and deposition. Particularly, the JCB's crater depth showed a high variation caused by a pronounced rim in the south compared to a less significant upraised rim in the north, and there was no general inference with respect to the other crater depths can be made.

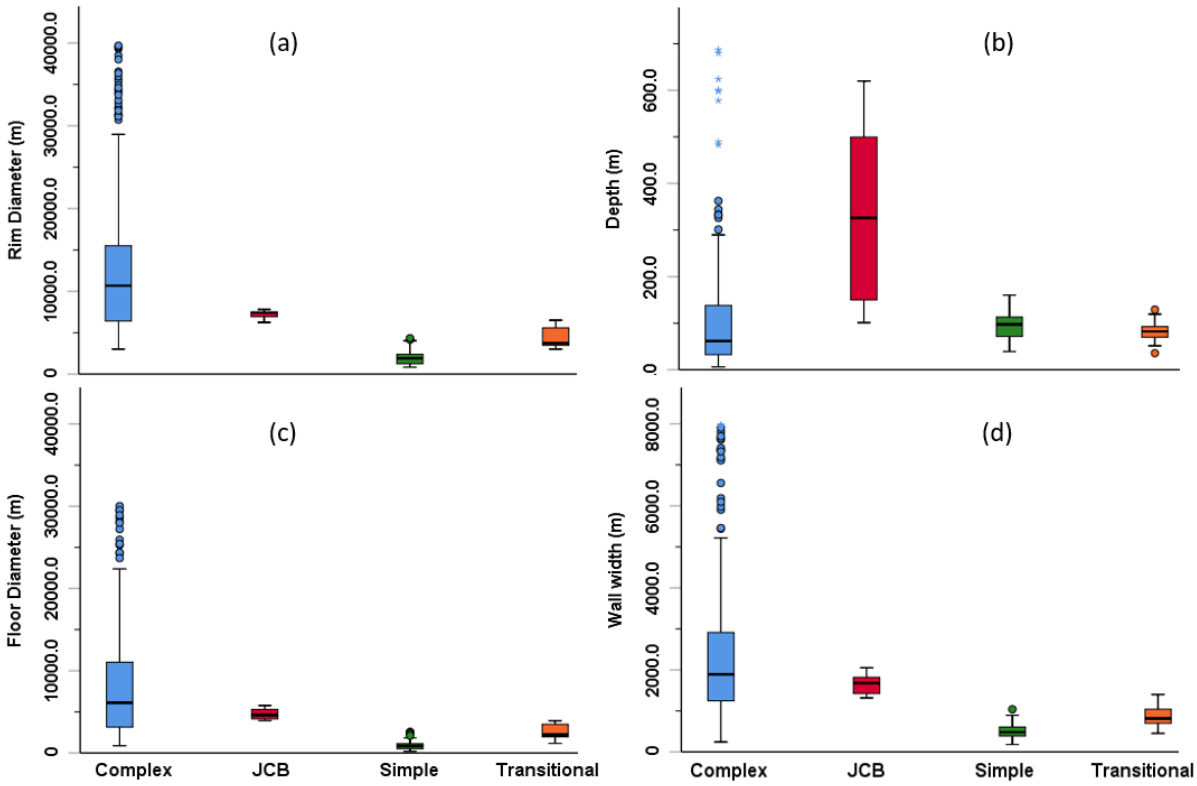

Figure 13. The box plots of (a) rim diameter, (b) crater depth, (c) floor diameter (d) wall width at different crater types together with JCB.

Furthermore, the relationship of morphometric parameters distribution between crater types have been visualized. The mean values of d and D, Df and D, and W and D were illustrated in scatter plots where each point represents the mean value of a single crater (Figure 14). Because the mean parameters of well preserved and moderately eroded craters for each type did don't show a major difference have been then merged. In general, the distribution of Df versus D, and W versus D showed high correlation for all three types (Figure 14b and c), while the high correlation observed for transitional impact craters were considered as statistical insignificant due to limited samples. The 3 transitional craters were found in between simple and complex craters (Figure 14a, b, c). The scatter plots well coincide with the distribution of individual morphometric parameters where simple craters are mainly concentrated in the lower left corner and complex craters are widely distributed over center to right upper corner. The similar variation trend of floor diameter with rim diameter has been also observed for lunar craters [29] where Df mainly increases as a function of rim diameter, despite other geological factors that might interfere the relationship, and also concluded that wall width increases with rim diameter as both are related with direct relationship [77, 78].

The distribution of d versus D in particular, did not show any relationship where a large dispersion was observed across the scatter plots (Figure 14a). The large scattered mean depths at various crater sizes could be associated with several factors including different target lithology, uneven mass transport to the crater floor, post impact sediment deposition, and post impact collapses of interior crater wall. Indeed, Boyce et al,. 2007 [86] reported that the impact craters in strong target are likely to be deeper as the strong targets reduce the amount of interior wall collapse while in weak targets the interior walls easily collapse under their own weight which could form shallow craters. In addition, a poor correlation of depth and diameter has been also reported for Pluto's Impact craters, where the complex crater showed high depth compared to simple craters [35]. It was therefore linked with different rheology between different areas and infilling materials [87], [88]. Based on the relative position of JCB impact crater, the JCB representative point falls within the complex cluster in all three figures (figure 14a, b, c). Therefore,

relative location of the mean parameter of floor diameter and wall width highly confirm that JCB could be belong to complex type.

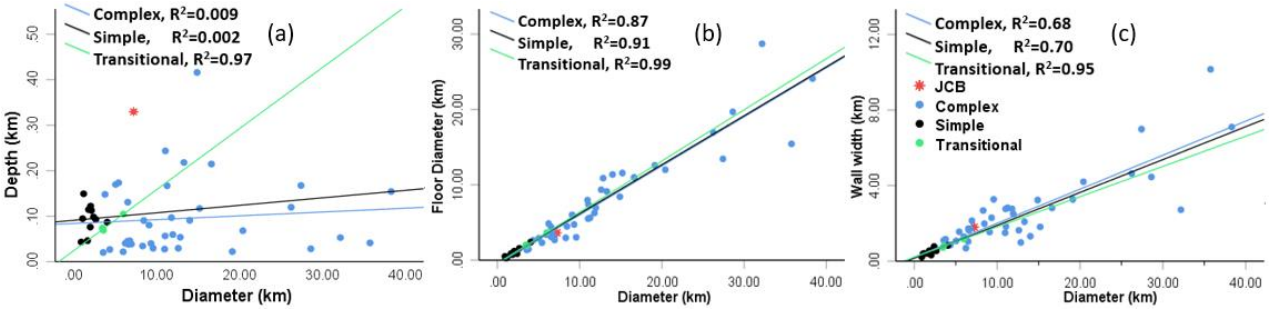

Figure 14. The scatter plots of mean parameters of impact craters (a) depth, (b) floor diameter, and (c) wall width against their rim diameters.

2.3.2. Hypothesis Statistical Analysis

The normal distribution of morphometric parameters; rim diameter (D), crater depth (d), floor diameter (Df), and wall width (W) was investigated based on Kolmogorov Smirnov test. The Kolmogorov Smirnov statistic values are within a range of 0.10 – 0.15 for simple and 0.13 – 0.17 for complex types, and p values were 0.00 – 0.018 and 0.00 for simple and complex craters, respectively. The results rejected the null hypothesis concluding that the morphometric parameters are not normally distributed for both types.

Because the parameters are not normally distributed, we used the Mann Whitney U test to analyze discernibility between simple and complex craters. The results indicated the difference between simple and complex craters in terms of that the rim diameter, floor diameter, and wall width. The mean ranks of rim diameter (45.27), floor diameter (48.38), and Wall width (51.20) for simple craters are significantly lower than rim diameter (238.0), floor diameter (237.12), and Wall width (236.32) of complex craters. In addition, the p values (0.00) and less than significant level (0.05) rejected the null hypothesis concluding statistical difference and classifiability between the simple and complex craters in terms of those three parameters. On the contrary, the mean ranks of crater depth showed a slight difference between simple (204.43) and complex craters (187.32), where the p values (0.2– 0.6) were greater than significant level (0.05) and retained the null hypothesis. It is then inferred that crater depth failed to statistically distinguish simple and complex crater types (Table 7a). Nevertheless, the complex impact craters are

generally deeper than simple craters, in the active geological conditions, the lithological properties and post impact modification could alter the apparent crater depth over time [86].

To figure out the crater type of JCB crater in terms of morphometric parameters one sample Wilcoxon Signed Rank Test was further conducted. The test revealed a significant difference between simple craters and JCB crater in terms of all morphometric parameters. The test statistics yielded 0.00 for all parameters between simple craters and JCB median values with p values range 0.005 – 0.008 (Table 7b). Conversely, the test between complex and JCB concluded that they are statistically similar for floor diameter and wall width (Table 7c). This result indicates that JCB crater is more likely similar to a complex type rather than a simple crater. However, the test indicated a difference between complex and JCB in terms of rim diameter and crater depth. It could be associated with the test method which is based on the central tendency testing with hypothesized value [30]. The median rim diameter of complex craters (10.6 km) is relatively higher than that of JCB (7.4km) which could be the reason for rejecting the rim diameter. In addition, the null hypothesis to reject the crater depth, could be explained by high JCB's crater depth compared to those of complex craters as well as dispersed crater depths observed a crossed all craters (Figure 13b). The previous studies reported JCB are relatively young craters, implying less exposure to the post impact modification processes showing relatively higher crater depth compared to both crater types. Indeed, Mann Whitney U test suggested that the crater depth cannot be used to distinguish crater types because they are more associated with the age of craters. Therefore, relaying on apparent crater depth which is highly subjected to the post-impact modification could lead to misinterpretation.

Table 7. The summary of the test statistics results (a) simple and complex (b) simple and JCB, (C) complex and JCB craters, where H0: Null hypothesis, Ref.p: Reference p value, and W.statistics: Wilcoxon statistics.

Mann Whitney U test, **H0**: The distribution of the data is the same across all crater types, at Ref. p =0.05				One Sample Wilcoxon Signed Test, **H0**: The median of the parameter is the same as the median of JCB, at Ref. p =0.05							
(a) Simple versus Complex,				(b) Simple craters versus JCB				(c) Complex craters versus JCB			
Parameters	Mean rank, Simple& Complex	P value	Decision	Parameters	W.statistics	P value	Decision	Parameters	W.statistics	P value	Decision
D	45.27& 238.0	0.00	Rejected	D	0.00	0.008	Rejected	D	607.0	0.001	Rejected
d	204.43& 187.32	0.2–0.6	Retained	d	0.00	0.008	Rejected	d	1.0	0	Rejected
Df	48.38& 237.12	0.00	Rejected	Df	0.00	0.005	Rejected	Df	502.0	0.055	Retained
W	51.2& 236.32	0.00	Rejected	W	0.00	0.008	Rejected	W	503.0	0.057	Retained

2.3.3. Random Forest Classification Assessment

An additional test on the separability of simple and complex craters was carried out by a random forest machine-learning algorithm. The classification results for validation data showed very good performance with an accuracy of 88.6% and a Kappa coefficient of 0.67 (Table 8a). However, a misclassification was observed for two complex craters (B.P. structure (Libya), 3.4 km and Steinheim (Germany), 3.8 km), where the model classified them as simple craters. As the figure 13 and 13 indicated, complex craters have wide distribution of morphometric parameters. They make a slight overlap with simple craters, and the cases in all parameters overlap would result in different types. Indeed, those craters have a slight overlap in ranges of 3.0 – 4.1 km, 0.8 – 2.5 km, and 0.2 – 1.0 km for rim diameter, floor diameter, and wall width, respectively. The RF classification confirms that the morphometric parameters can be useful to define specific types of impact craters except for the rare cases of overlap.

As the RF classification is confirmed to be a useful technic to preliminarily define impact crater type, so JCB crater was tested with the same method. In the case of JCB was assumed to be a simple crater, the model classified it as a complex. The other case assumed JCB as complex, the model also classified as complex type. Thus, in both assumptions the model classified JCB as complex crater. In addition, in both cases, the model kept misclassifying the two mentioned above complex craters as simple craters. Compared to the similar-sized craters, the JCB is not alone in lacking central uplift on the surface, Bigach, (Kazakhstan), 8 km; Ragozinka crater, (Russia), 9 km; and Middlesboro, (USA), 6 km, moderately eroded and central uplifts overlain with infill deposits [2]. Therefore, the JCB crater could be a moderately eroded complex crater, where the central uplift is confined in lacustrine sediments. These results are consistent with box plots, scatter plots, and statistical tests.

Table 8. Accuracy assessment of crater types where User's Accuracy, and Production's Accuracy (PA) for each type are presented.

(a) Simple versus complex craters TESTING (14 Complex & 4 Simple)			(b) Including JCB as simple crater TESTING (14 Complex & 5 Simple)		(c) Including JCB as complex crater TESTING (15 Complex & 4 Simple)	
Classes	**Complex**	**Simple**	**Complex**	**Simple**	**Complex**	**Simple**
Complex	12	0	12	1	13	0
Simple	2	4	2	4	2	4
PA (%)	85.7	100	85.7	80	86.7	100
UA (%)	100	66.7	92.3	66.7	100	66.7
Overall Accuracy (%)	88.6		84.3		89.8	
Kappa	0.67		0.55		0.68	

Furthermore, the important variables for the classification of impact crater types, have been identified and ranked by Mean Decrease Gini (MDG) and Mean Decrease Accuracy (MDA) indices (Figure 15). The rim diameter was ranked first followed by floor diameter and wall width, while the crater depth below the sharp decrease in mean accuracy played the least role inferring low discernibility. This observation coincides well with scatter plot and box plot analysis results. Moreover, the results agreed with statistical tests which concluded those three parameters are statistically very useful for discerning simple and complex craters. The complex craters have larger rim diameter, floor diameter, and wall width. The higher energy impact crating complex craters make larger rim diameters in general. Moreover, the complex craters mostly have flat bases while the simple craters have parabolic bases. Thus, along with the association of rim diameter, the floor diameters of complex craters are larger than simple craters [87]. In addition, the large wall width observed for most complex craters are explained with a large terraced wall rim and modification process that mostly occur on large craters [35]. Indeed, terraces mostly occur in complex craters because of the weakness of target lithology that induce circumferentially fracturing of the crater rim [88].

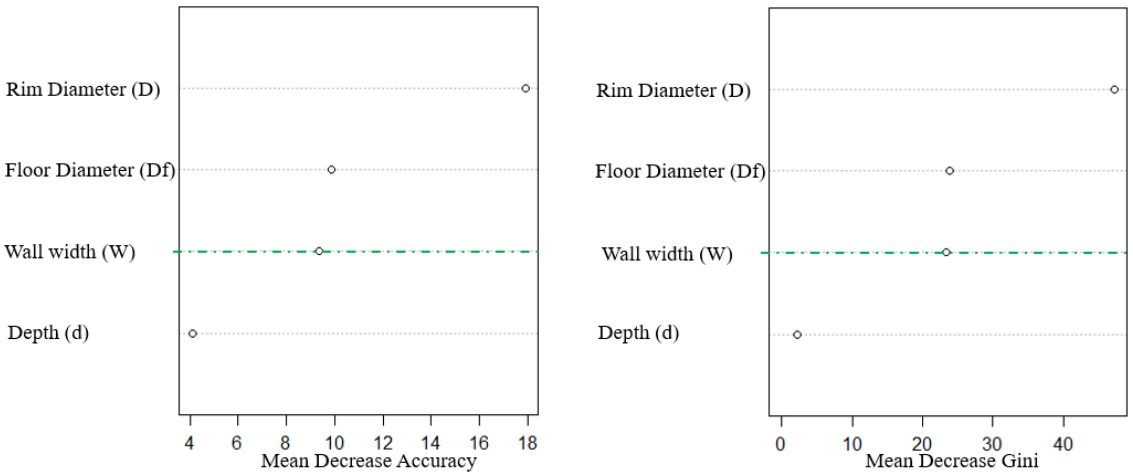

Figure 15. The illustration of variable importance of morphometric parameters, based on MDA and Gini indices.

This study tested the quantitative effectiveness of morphometric parameters extracted from remote sensing data to classify different types of terrestrial impact craters using various statistical methods and machine learning classification. The results confirmed that complex and simple craters can be statistically distinguished in terms of the three morphometric parameters, rim diameter, floor width, and wall diameter. Moreover, those parameters were applied to the recent discovered JCB impact crater and figured out the JCB crater shows morphometric characteristics of complex terrestrial impact craters. This study is the first study attempted to evaluate the applicability of morphometric parameters for identifying defining terrestrial impact crater types. It infers that if any crater is found, a preliminary test using morphometric parameters can provide important clues for impact crater types. Indeed, if this method is combined with [68], which introduced object oriented remote sensing approaches for detection of terrestrial impact craters, detection of impact craters and identification of crater type can be achieved with remote sensing methods at a reconnaissance survey. However, this study only used impact craters that morphological parameters are extractable from remote sensing data, and, thus, this method can be applied to younger impact craters. Moreover, more confirmed impact craters need to be added for the derivation of classification for transitional impact craters.

2.4. Conclusion

This study first introduced the dissimilarity analysis of morphometric parameters for different types of terrestrial impact craters. It approved that using global raster topographic data, and analysis of morphometric parameters could be an alternative remote sensing approach to decide a provisional crater types. Advanced geophysical or drilling operations must proceed to finally confirm the crater type. The study reported the analysis of dissimilarity in morphometric parameters of 53 well and moderately eroded terrestrial impact craters with diameter size lie within 0.88 – 40 km. The sample data was limited by exposure status, and resolution of SRTM DEM, thus this approach can be relevant for the less modified craters including well-preserved, moderately eroded craters and greater than 0.8 km in rim diameter.

There was no significant difference observed based on exposure status due to a limited sample of well-preserved craters. However, the study revealed a significant difference between crater types namely simple and complex craters in terms of three morphometric parameters. The statistical distribution of morphometric parameters showed less overlapping between different crater types, where the rim diameter, floor diameter, and wall width of complex craters were generally found higher than those of simple craters. However, crater depth showed high overlapping across all crater types. Regarding the morphometric parameters of JCB, they have been characterized by rim diameter (6.2 – 7.8 km), floor diameter (3.9 – 5.3 km), wall width (1.3 – 2.05 km), which showed an overlap with those of complex craters and relatively higher than those of simple craters.

We introduced the first trial of analyzing the separability between simple and complex craters based on a non-parametric Mann Whitney U test at a reference of a significant level of 0.05. The null hypothesis assuming the distribution of the morphometric parameters is the same across both simple and complex types was rejected for three parameters including rim diameter, floor diameter, and wall width concluding that both types are different. The significant difference was justified by large rim diameter, flat crater floor, and wide crater wall width mostly found for complex craters compared to narrow parabolic bases characterize simple craters. However, the null hypothesis was retained for crater depth, which statistically means that it is not possible to separate simple craters from complex craters in terms of their depths. Crater depth showed high

inconsistency across different crater types which is likely due to different post impact modification effects, so relying on it could lead to misinterpretations. In addition, one sample one sample Wilcoxon Signed Rank Test statistic indicated no relationships of JCB parameters with those of simple craters. However, an association of JCB with complex was observed for floor diameter and wall width parameters at a significant level of 0.05.

Furthermore, the Random Forest effectively approved the discernability of simple and complex craters with a high overall accuracy of 88.6 % and a Kappa coefficient of 0.67. Besides, assuming JCB as complex in testing dataset improved the overall accuracy and Kappa Coefficient to 89.8 % and 0.68, respectively. However, assuming JCB as simple has decreased the overall accuracy and Kappa coefficient to 84.3 % and 0.55 respectively. Thus, an increase in accuracy for the assumption of complex type could indicate that morphometric parameters of JCB are likely more associated with those of complex craters rather than simple craters. The morphometric parameters that played a major role in this classification included rim diameter floor diameter and wall width and are consistent with Mann Whitney U test results that showed significant differences between simple and complex craters. Therefore, the consistent results of RF important parameters, statistical test, and statistical distribution (figure 13) indicated that morphometric parameters could be easy alternative approaches for defining simple craters from complex craters at preliminary stage. Moreover, considering other similar-sized moderately eroded complex craters said above, showed a lack of central uplift on the surface, the provisional crater type of JCB could be moderately complex craters rather than a simple crater.

EPILOGUE

Impact craters serve as a paramount /profound geological information repository about planetary evolution. The formation processes biased worldwide distribution, and impressive landscape of impact craters have motivated various scientists to explore the common characteristics of well-known impact craters thereby identifying the new possible craters. This study aimed at introducing object-oriented remote sensing approaches for the detection of terrestrial impact craters, and identification of crater types based on morphometric parameters at a preliminary exploration stage. The multiresolution segmentation of integrated four morphometric layers including digital elevation model, slope, aspect, and hillshade layers at different scale parameters detected the upraised circular topographic imprints of rim craters (chapter 1). Furthermore, the morphometric parameters extracted from the digital elevation model showed a significant difference between simple and complex craters (chapter 2).

Chapter 1 showed the possibility of a remote sensing approach to detecting impact craters via object-oriented segmentation. The integration of different morphometric layers enhanced the topographic contrast compared to one layer during the segmentation process. The user-defined scale parameters solved the hindrance of detecting impact craters of different sizes. The eight optimum scale parameters provided in this study showed a good correlation (R^2=0.78) with rim diameters of 70 detected impact craters ranging within 0.88 – 70 km diameter size. The object-oriented random forest machine learning algorithm revealed the discernability of impact craters and common analogous features such as volcanic calderas and common landscape features associated with mountainous areas namely valleys. The violin plots presented a quantitative significant difference in medians for geometric, topographic, and texture-attributes of detected impact craters with those of volcanic calderas and valleys. In general, the detected impact craters were characterized by circular jagged objects compared to relatively circular smooth objects of volcanic calderas and elongated objects of valleys. The jaggedness of impact crater objects has been explained by relatively weak, fractured, and brecciated materials that mostly form the crater rims which are easily subjected to erosion compared to igneous volcanic rocks mostly formed caldera rims. In addition, the post deformation of impact craters, including inward collapse, slump of rims, lower the

elevation, relief and circularity with time compared to volcanic calderas formed by collapse of underground, emptying the magma and inducing ground sinking over time.

Chapter 2 proved the applicability of morphometric parameters in defining terrestrial crater types via statistical tests and machine learning algorithms. The box and scatter plots visualized the quantitative distribution of four common morphometric parameters representing simple, complex, and transition craters, and showed that rim diameter, floor diameter, and wall width indicated a significant difference across different types with slight overlap. However, crater depth showed a significant overlap across all crater types. In addition, Mann Whitney U test revealed a significant difference between simple and complex in terms of three parameters including rim diameter floor diameter, and wall width, while depth did not show any difference. The random forest algorithm effectively proved the separability of simple and complex craters based on morphometric parameters, with a higher overall accuracy of 88.6 % and a Kappa coefficient of 0.67. The morphometric parameters that played a major role in separating simple and complex consisted of those found by statistical tests and showed even less of overlapping in box plots. In general, the size of the impact crater is mainly controlled by the energy of the impactor, complex craters mostly originate from a higher energy impactor that cause a wide modification of the earth's crust and vice versa. In addition, complex craters are mostly characterized by large flat bases compared to the narrow parabolic shape of simple craters. Moreover, the large, terraced wall mostly occurs in complex craters because of the weakness of target lithology that induces circumferentially fracturing of the crater rim causing a relatively wider wall width than simple craters. However, the crater depth was found as mostly subjected to erosion parameters, relaying on it could lead to misinterpretation.

Therefore, implementing those two chapters could lead to the identification of possible new crater candidates in remote areas, and define their associated crater types at the preliminary stage of exploration. This could contribute to the discovery of new candidates and serve as a guide for further geological surveys for ultimate impact crater evidences.

PUBLICATIONS

Chapter 1

Emmanuel, H., Yu, J., Wang, L., Choi, S. H., & Rwatangabo, D. E. R. (2023). Object-Oriented Remote Sensing Approaches for the Detection of Terrestrial Impact Craters as a Reconnaissance Survey. *Remote Sensing*, *15*(15). https://doi.org/10.3390/rs15153807

REFERENCES

1. Bruzzone L, Lizzi L, Marchetti PG, Earl J, Milnes M. Recognition and detection of impact craters from EO products. Eur Sp Agency, (Special Publ ESA SP. 2004;(553):85–92.
2. Ishak B. Encyclopedic atlas of terrestrial impact craters. Vol. 60, Contemporary Physics. 2019. 330–330 p.
3. Grieve RAF, Therriault AM. Observations at terrestrial impact structures: Their utility in constraining crater formation. Meteorit Planet Sci. 2004;39(2):199–216.
4. Kennedy J, Alanís RM. Book Review. Carbohydr Polym. 2005;62(1):87.
5. Schmieder M, Kring DA. Earth's Impact Events through Geologic Time: A List of Recommended Ages for Terrestrial Impact Structures and Deposits. Astrobiology. 2020;20(1):91–141.
6. Le Feuvre M, Wieczorek MA. Nonuniform cratering of the terrestrial planets. Icarus. 2008;197(1):291–306.
7. Kenkmann T. The terrestrial impact crater record: A statistical analysis of morphologies, structures, ages, lithologies, and more. Meteorit Planet Sci. 2021;56(5):1024–70.
8. Crósta AP, Reimold WU, Vasconcelos MAR, Hauser N, Oliveira GJG, Maziviero M V., et al. Impact cratering: The South American record – Part 1. Chemie der Erde [Internet]. 2019;79(1):1–61. Available from: https://doi.org/10.1016/j.chemer.2018.06.001
9. Lobpries TA, Lapen TJ. Remote sensing evidence for a possible 10 kilometer in diameter impact structure in north-central Niger. J African Earth Sci [Internet]. 2019;150(May 2018):673–84. Available from: https://doi.org/10.1016/j.jafrearsci.2018.09.020
10. Reimold WU, Koeberl C. Impact structures in Africa: A review. J African Earth Sci[Internet].2014;93:57–175.Availablefrom: http://dx.doi.org/10.1016/j.jafrearsci.2014.01.008
11. Wright SP, Tornabene LL, Ramsey MS. Remote Sensing of Impact Craters. Impact Cratering Process Prod. 2012;194–210.
12. Mansouri Daneshvar MR. Remote sensing analysis for the possible impact structure of Lakhčak Crater in southern Afghanistan. Appl Geomatics. 2015;7(4):275–82.
13. Scholz CA, Karp T, Lyons RP. Structure and morphology of the Bosumtwi impact structure from seismic reflection data. Meteorit Planet Sci. 2007;42(4–5):549–60.
14. Vasconcelos MAR, Crósta AP, Molina EC. Geophysical characteristics of four possible impact structures in the Parnaíba Basin, Brazil: Comparison and implications. Spec Pap Geol Soc Am. 2010;465(December 2015):201–17.
15. Lobpries TA, Lapen TJ. Remote sensing evidence for a possible 10 kilometer in

diameter impact structure in north-central Niger. J African Earth Sci [Internet]. 2019;150(October 2018):673–84. Available from: https://doi.org/10.1016/j.jafrearsci.2018.09.020

16. Theilen-Willige B. Morphometric and Structural Evaluations of Satellite Data from the Bosumtwi Impact Structure and Adjacent Areas in Ashanti, Ghana. Eur J Environ Earth Sci. 2021;2(3):7–14.

17. Wang XY, Luo L, Guo HD, Mu LL, Li C, Ji W, et al. Cratering process and morphological features of the Xiuyan impact crater in Northeast China. Sci China Earth Sci. 2013;56(10):1629–38.

18. Crósta AP, Kazzuo-Vieira C, Pitarello L, Koeberl C, Kenkmann T. Geology and impact features of Vargeão Dome, southern Brazil. Meteorit Planet Sci. 2012;47(1):51–71.

19. Maziviero M V., Vasconcelos MAR, Crósta AP, Góes AM, Reimold WU, De C. Carneiro C. Geology and impact features of Riachão structure, northern Brazil. Meteorit Planet Sci. 2013;48(10):2044–58.

20. Williams GE, Gostin VA. Geomorphology of the Acraman impact structure, Gawler Ranges, South Australia. Cad do Lab Xeol Laxe. 2010;35(35):209–19.

21. Vamshi GT, Martha TR, Vinod Kumar K. An object-based classification method for automatic detection of lunar impact craters from topographic data. Adv Sp Res [Internet]. 2016;57(9):1978–88. Available from: http://dx.doi.org/10.1016/j.asr.2016.01.022

22. Sawabe Y, Matsunaga T, Rokugawa S. Automated detection and classification of lunar craters using multiple approaches. Adv Sp Res. 2006;37(1):21–7.

23. Urbach ER, Stepinski TF. Automatic detection of sub-km craters in high resolution planetary images. Planet Space Sci. 2009;57(7):880–7.

24. Salamunićcar G, Lonarić S, Pina P, Bandeira L, Saraiva J. MA130301GT catalogue of Martian impact craters and advanced evaluation of crater detection algorithms using diverse topography and image datasets. Planet Space Sci. 2011;59(1):111–31.

25. Masaitis VL. Morphological, structural and lithological records of terrestrial impacts: An overview. Aust J Earth Sci. 2005;52(4–5):509–28.

26. Li W, Zhou B, Hsu CY, Li Y, Ren F. Recognizing terrain features on terrestrial surface using a deep learning model - An example with crater detection. Proc 1st Work GeoAI AI Deep Learn Geogr Knowl Discov GeoAI 2017. 2017;33–6.

27. Grieve RAF. Economic natural resource deposits at terrestrial impact structures. Geol Soc Spec Publ. 2005;248(1994):1–29.

28. Turtle EP, Pierazzo E, Collins GS, Osinski GR, Melosh HJ, Morgan J V., et al. Impact structures: What does crater diameter mean? Spec Pap Geol Soc Am. 2005;384:1–24.

29. Osinski GR, Silber EA, Clayton J, Grieve RAF, Hansen K, Johnson CL, et al. Transitional impact craters on the Moon: Insight into the effect of target lithology

on the impact cratering process. Meteorit Planet Sci. 2019;54(3):573–91.

30. Acocella V. Regional and local tectonics at Erta Ale caldera, Afar (Ethiopia). J Struct Geol. 2006;28(10):1808–20.

31. Thouret JC. Volcanic geomorphology-an overview. Earth Sci Rev. 1999;47(1–2):95–131.

32. Carrión-Mero P, Montalván-Burbano N, Paz-Salas N, Morante-Carballo F. Volcanic geomorphology: A review of worldwide research. Geosci. 2020;10(9):1–17.

33. Survey USG. USGS [Internet]. Available from: https://earthexplorer.usgs.gov

34. GVB-CSIC. CCDB [Internet]. Available from: https://gvb-csic.es/CCDB/

35. Trimble. Trimble Documentation: eCognition ® Developer User Guide. 2018;(March):1–272.

36. Drăguţ L, Eisank C. Automated object-based classification of topography from SRTM data. Geomorphology. 2012;141–142:21–33.

37. Hölbling D, Füreder P, Antolini F, Cigna F, Casagli N, Lang S. A semi-automated object-based approach for landslide detection validated by persistent scatterer interferometry measures and landslide inventories. Remote Sens. 2012;4(5):1310–36.

38. Ma L, Li M, Ma X, Cheng L, Du P, Liu Y. A review of supervised object-based land-cover image classification. ISPRS J Photogramm Remote Sens [Internet]. 2017;130:277–93. Available from: https://doi.org/10.1016/j.isprsjprs.2017.06.001

39. Martha TR, Kerle N, Jetten V, van Westen CJ, Kumar KV. Characterising spectral, spatial and morphometric properties of landslides for semi-automatic detection using object-oriented methods. Geomorphology [Internet]. 2010;116(1–2):24–36. Available from: http://dx.doi.org/10.1016/j.geomorph.2009.10.004

40. Lucieer A, Stein A. Existential uncertainty of spatial objects segmented from satellite sensor imagery. IEEE Trans Geosci Remote Sens. 2002;40(11):2518–21.

41. El-naggar AM. Determination of optimum segmentation parameter values for extracting building from remote sensing images. Alexandria Eng J [Internet]. 2018;57(4):3089–97. Available from: https://doi.org/10.1016/j.aej.2018.10.001

42. Yang J, He Y, Caspersen J, Jones T. A discrepancy measure for segmentation evaluation from the perspective of object recognition. ISPRS J Photogramm Remote Sens [Internet]. 2015;101:186–92. Available from: http://dx.doi.org/10.1016/j.isprsjprs.2014.12.015

43. Li P, Song B, Guo J, Xiao X. A Multilevel Hierarchical Image Segmentation Method for Urban Impervious Surface Mapping Using Very High Resolution Imagery. IEEE J Sel Top Appl Earth Obs Remote Sens. 2011;4(1):103–16.

44. DeFries RS, Chan JCW. Multiple criteria for evaluating machine learning algorithms for land cover classification from satellite data. Remote Sens Environ. 2000;74(3):503–15.

45. Castillejo-González IL, Angueira C, García-Ferrer A, Orden MS de la. Combining object-based image analysis with topographic data for landform mapping: A case study in the semi-arid Chaco ecosystem, Argentina. ISPRS Int J Geo-Information. 2019;8(3).

46. Olaya V, Conrad O. Geomorphometry in SAGA. Vol. 33, Developments in Soil Science. 2009. 293–308 p.

47. Van Den Eeckhaut M, Poesen J, Verstraeten G, Vanacker V, Moeyersons J, Nyssen J, et al. The effectiveness of hillshade maps and expert knowledge in mapping old deep-seated landslides. Geomorphology. 2005;67(3–4):351–63.

48. Wilson JP, Gallant JC. Terrain analysis : principles and applications / edited by John P. Wilson, John C. Gallant [Internet]. 2000. p. 520. Available from: https://www.wiley.com/en-ie/Terrain+Analysis:+Principles+and+Applications-p-9780471321880

49. Na J, Ding H, Zhao W, Liu K, Tang G, Pfeifer N. Object-based large-scale terrain classification combined with segmentation optimization and terrain features: A case study in China. Trans GIS. 2021;25(6):2939–62.

50. Takashimizu Y, Iiyoshi M. New parameter of roundness R: circularity corrected by aspect ratio. Prog Earth Planet Sci [Internet]. 2016;3(1). Available from: http://dx.doi.org/10.1186/s40645-015-0078-x

51. Laliberte AS, Rango A. Texture and scale in object-based analysis of subdecimeter resolution unmanned aerial vehicle (UAV) imagery. IEEE Trans Geosci Remote Sens. 2009;47(3):761–70.

52. Mason BG, Pyle DM, Oppenheimer C. The size and frequency of the largest explosive eruptions on Earth. Bull Volcanol. 2004;66(8):735–48.

53. Tsikalas F, Faleide JI. Post-impact structural crater modification due to sediment loading: An overlooked process. Meteorit Planet Sci. 2007;42(11):2013–29.

54. Cole JW, Milner DM, Spinks KD. Calderas and caldera structures: A review. Earth-Science Rev. 2005;69(1–2):1–26.

55. Mouginis-Mark PJ, Rowland SK. The geomorphology of planetary calderas. Geomorphology. 2001;37(3–4):201–23.

56. Kriger - Deriving Morphometric Parameters and the Simple-to-Complex Transition Diameter From a_2018.pdf.

57. Schmincke H. Cyclic caldera collapse : Piston or piecemeal subsidence ? Field and experimental evidence. 2002;(2):135–8.

58. McCall GJH. Half a century of progress in research on terrestrial impact structures: A review. Earth-Science Rev [Internet]. 2009;92(3–4):99–116. Available from: http://dx.doi.org/10.1016/j.earscirev.2008.11.004

59. Grosse P, van Wyk de Vries B, Euillades PA, Kervyn M, Petrinovic IA. Systematic morphometric characterization of volcanic edifices using digital elevation models. Geomorphology. 2012;136(1):114–31.

60. S. Choi, S. W. Kim, E. K. Choi, and Y. C. Lee, “Estimating the impact process of the Jeokjung-Chogye Basin in Korea from gravity field interpretation,” *Geophys. J. Int.*, vol. 228, no. 2, pp. 1457–1463, 2022.

61. J. Lim, S. S. Hong, M. Han, S. Yi, and S. W. Kim, “First finding of impact cratering in the Korean Peninsula,” *Gondwana Res.*, vol. 91, pp. 121–128, 2021.

62. S. H. Choi, J. H. Lee, S. S. Kim, J. Yu, and I. S. Puchtel, “Meteoritic component in impact breccias of the Jeokjung-Chogye structure, South Korea: Evidence from the HSE abundances and Re[sbnd]Os isotopic systematics,” *Chem. Geol.*, vol. 613, no. September, p. 121145, 2022.

63. V. J. Bray, G. S. Collins, J. V. Morgan, and P. M. Schenk, “The effect of target properties on crater morphology: Comparison of central peak craters on the Moon and Ganymede,” *Meteorit. Planet. Sci.*, vol. 43, no. 12, pp. 1979–1992, 2008.

64. M. Schmieder, H. Seyfried, and O. Gerel, “The circular uneged uul structure (east gobi basin, mongolia) - geomorphic and structural evidence for meteorite impact into an unconsolidated coarse-clastic target?,” *J. Asian Earth Sci.*, vol. 64, pp. 58–76, 2013.

65. E. M. Ghoneim, “Ibn-Batutah: A possible simple impact structure in southeastern Libya, a remote sensing study,” *Geomorphology*, vol. 103, no. 3, pp. 341–350, 2009.

66. T. Kenkmann, M. A. R. Vasconcelos, A. P. Crósta, and W. U. Reimold, “The complex impact structure Serra da Cangalha, Tocantins State, Brazil,” *Meteorit. Planet. Sci.*, vol. 46, no. 6, pp. 875–889, 2011.

67. Q. Sun, W. Fa, M.-H. Zhu, and J. Du, “Morphological characteristics of impact craters with diameters of 5–20 km on the Moon,” *Icarus*, vol. 404, no. October 2022, p. 115688, 2023.

68. H. Emmanuel, J. Yu, L. Wang, S. H. Choi, and D. E. R. Rwatangabo, “Object-Oriented Remote Sensing Approaches for the Detection of Terrestrial Impact Craters as a Reconnaissance Survey,” *Remote Sens.*, vol. 15, no. 15, 2023.

69. S. J. Robbins *et al.*, “Depths of Pluto’s and Charon’s craters, and their simple-to-complex transition,” *Icarus*, vol. 356, no. June 2020, p. 113902, 2021.

70. M. Gottwald, T. Fritz, H. Breit, B. Schättler, and A. Harris, “Remote sensing of terrestrial impact craters: The TanDEM-X digital elevation model,” *Meteorit. Planet. Sci.*, vol. 52, no. 7, pp. 1412–1427, 2017.

71. R. A. F. Grieve and M. Pilkington, “The signature of terrestrial impacts,” *AGSO J. Aust. Geol. Geophys.*, vol. 16, no. 4, pp. 399–420, 1996.

72. J. Kalynn, C. L. Johnson, G. R. Osinski, and O. Barnouin, “Topographic characterization of lunar complex craters,” *Geophys. Res. Lett.*, vol. 40, no. 1, pp. 38–42, 2013.

73. A. P. Crósta *et al.*, “Impact cratering: The South American record – Part 1,” *Chemie der Erde*, vol. 79, no. 1, pp. 1–61, 2019.

74. A. P. Crósta *et al.*, "Impact cratering: The South American record—Part 2," *Chemie der Erde*, vol. 79, no. 2, pp. 191–220, 2019.

75. P. W. Haines, "Impact cratering and distal ejecta: The Australian record," *Aust. J. Earth Sci.*, vol. 52, no. 4–5, pp. 481–507, 2005.

76. V. L. Masaitis, "Impact structures of northeastern Eurasia: The territories of Russia and adjacent countries," *Meteorit. Planet. Sci.*, vol. 34, no. 5, pp. 691–711, 1999.

77. S. Vijayan, K. Vani, and S. Sanjeevi, "Topographical analysis of lunar impact craters using SELENE images," *Adv. Sp. Res.*, vol. 52, no. 7, pp. 1221–1236, 2013.

78. M. Chen, M. Lei, D. Liu, Y. Zhou, H. Zhao, and K. Qian, "Morphological features-based descriptive index system for lunar impact craters," *ISPRS Int. J. Geo-Information*, vol. 7, no. 1, 2018.

79. D. M. H. Baker and J. W. Head, "New morphometric measurements of craters and basins on Mercury and the Moon from MESSENGER and LRO altimetry and image data: An observational framework for evaluating models of peak-ring basin formation," *Planet. Space Sci.*, vol. 86, pp. 91–116, 2013.

80. B. Gerald, "A Brief Review of Independent, Dependent and One Sample t-test," *Int. J. Appl. Math. Theor. Phys.*, vol. 4, no. 2, p. 50, 2018.

81. N. Nachar, "The Mann-Whitney U: A Test for Assessing Whether Two Independent Samples Come from the Same Distribution," *Tutor. Quant. Methods Psychol.*, vol. 4, no. 1, pp. 13–20, 2008.

82. E. Ostertagová, O. Ostertag, and J. Kováč, "Methodology and application of the Kruskal-Wallis test," *Appl. Mech. Mater.*, vol. 611, no. August 2014, pp. 115–120, 2014.

83. Usman, "Mathematical Theory and Modeling Power Efficiency of Sign Test and Wilcoxon Signed Rank Test Relative to T-Test," *Issn*, vol. 5, no. 12, pp. 2224–5804, 2015.

84. Q. Sun, W. Fa, M. H. Zhu, and J. Du, "Morphological characteristics of impact craters with diameters of 5–20 km on the Moon," *Icarus*, vol. 404, no. October 2022, p. 115688, 2023.

85. J. M. Boyce and H. Garbeil, "Geometric relationships of pristine Martian complex impact craters, and their implications to Mars geologic history," *Geophys. Res. Lett.*, vol. 34, no. 16, pp. 1–5, 2007.

86. J. M. Boyce, P. Mouginis-Mark, H. Garbeil, and L. L. Tornabene, "Deep impact craters in the Isidis and southwestern Utopia Planitia regions of Mars: High target material strength as a possible cause," *Geophys. Res. Lett.*, vol. 33, no. 6, pp. 2–5, 2006.

87. C. V. N. Villaça, A. P. Crósta, and C. H. Grohmann, "Morphometric analysis of pluto's impact craters," *Remote Sens.*, vol. 13, no. 3, pp. 1–18, 2021.

88. S. J. Robbins and B. M. Hynek, "A new global database of Mars impact craters

≥1 km: 1. Database creation, properties, and parameters," *J. Geophys. Res. Planets*, vol. 117, no. 5, pp. 1–18, 2012.

APPENDICES

Table A1. The confirmed and exposed terrestrial impact craters used in this study were collected from encyclopedic atlas of

terrestrial impact craters [2,7].

Impact Crater	Country	Latitude	Longitude	ID	Diameter (km)	Exposure	Target Lithology	Type	Ages (ma)
Dhala	India	25.298	78.142	I01	12	ex, pc	Crystalline	C	1700–2500
Sierra Madera	USA	30.596	-102.912	I02	12	ex, pc	Sandstone	C	100
Gweni-Fada	Chad	17.421	21.755	I03	14–22	ex, pc	Sandstone	C	355
Bigach	Kazakhstan	48.568	82.036	I04	8	ex, pc	Mixed	C	3 – 5
Meteor Crater	USA	35.027	-111.023	I05	1.2	ex, pc	Sandstone	S	0.05
Ramgarh	India	25.335	76.624	I06	10.2	ex, pc	Sandstone	C	165
Cerro do Jarao	Brazil	-30.211	-56.539	I07	13	ex, smor	Sandstone	C	137
Connolly Basin	Australia	-23.538	124.761	I08	9	ex, pc	Sandstone	C	55–75
Tenoumer	Mauritania	22.918	-10.405	I09	1.9	ex, pc	Mixed	S	1.52
Piccaninny	Australia	-17.420	128.438	I10	7	ex, smor	Sandstone	C	360
Chogye	SouthKorea	35.537	128.269	I11	7	ex, pc	Sandstone	C	0.03–0.06
Vargeao Dome	Brazil	-26.805	-52.164	I12	12.4	ex	Sandstone	C	137
Mien	Sweden	56.431	14.856	I13	9	ex, sub	Crystalline	C	118.7
Gow	Canada	56.453	-104.482	I15	5	ex, sub	Crystalline	C	250
Santa Marta	Brazil	-10.167	-45.233	I16	10	ex, pc	Sandstone	C	93
Acraman	Australia	-32.017	135.450	I17	40–85	ex, sub	Crystalline	C	580
Gosses Bluff	Australia	-23.817	132.308	I18	22	ex, pc	Sandstone	C	142
Upheaval Dome	USA	38.433	-109.928	I20	6	ex	Sandstone	C	66–100
Foelsche	Australia	-16.676	136.784	I21	6	ex, pc	Sandstone	C	541–981
Jebel Waqf as Suwwan	Jordan	31.039	36.807	I22	6.1	ex, pc	Sandstone	C	37
Agoudal	Morocco	31.996	-5.516	I24	2.8	ex	Sandstone	C	0.3
Aorounga	Chad	19.084	19.244	I25	12.6–16	ex	Sandstone	C	355
Decaturville	USA	37.890	-92.720	I26	6	ex, pc	Sandstone	C	300
Bosumtwi	Ghana	6.500	-1.408	I27	10.5	ex, sub	Mixed	C	1.07
Decorah	USA	43.300	-91.772	I29	5.6	pc	Sandstone	T	460–483
Ouarkziz	Algeria	29.004	-7.551	I30	3.5	ex, pc	Sandstone	T	66
Zhamanshin	Kazakhstan	48.350	60.937	I32	14	ex, pc	mixed	C	0.75–1.1
Oasis	Libya	24.572	24.412	I33	5.2–18	ex, pc	Sandstone	C	120
Serra da Cangalha	Brazil	-8.082	-46.857	I34	13.7	ex	Crystalline	C	300
La Moinerie	Canada	57.440	-66.586	I35	8	ex, sub	Crystalline	C	400
Middlesboro	USA	36.631	-83.728	I36	6	ex	Sandstone	C	290–300
Colonia	Brazil	-23.880	-46.706	I37	3.6	ex, pc	Crystalline	T	5 – 36
Vista-Alegre	Brazil	-25.961	-52.690	I38	9.5	ex	Mixed	C	111–134
B.P. structure	Libya	25.318	24.310	I40	3.4	ex	Sandstone	C	120
Ragozinka	Russia	58.706	61.797	I41	9	ex, pc	mixed	C	50

Goyder	Australia	-13.477	135.040	I43	3	ex, pc	Sandstone	C	150–1400
Chiyli	Kazakhstan	49.177	57.834	I44	5.5	ex, pc	Sandstone	C	5.5
Lonar	India	19.974	76.509	I46	1.88	ex, sub	Crystalline	S	0.57
Wetumpka	USA	32.525	-86.176	I47	7	ex	Crystalline	C	84
Karakul	Tajikistan	39.067	73.433	I48	52	ex, smor	Mixed	C	50 – 5
Pantasma	Nicaragua	13.365	-85.954	I49	14	ex	Crystalline	C	0.8
Shunak	Kazakhstan	47.207	72.761	I50	2.8	ex, pc	Crystalline	S	34
Deep Bay	Canada	56.415	-102.983	I51	13	ex, sub	Crystalline	C	95–102
Crawford	Australia	-34.728	139.033	I53	8.5	ex	Crystalline	C	32 – 38
Talemzane	Algeria	33.315	4.034	I54	1.75	ex, pc	Sandstone	S	0.5 – 3
Xiuyan	China	40.364	123.460	I57	1.8	ex, pc	Crystalline	S	0.05
Goat Paddock	Australia	-18.348	126.677	I61	5	ex, pc	Sandstone	T	56 – 64
Tin Bider	Algeria	27.600	5.112	I62	6	ex, pc	Sandstone	C	50
Clearwater west	Canada	56.211	-74.500	I63	32	ex, sub	Mixed	C	290–300
Clearwater East	Canada	56.064	-74.083	I64	24	ex, sub	Mixed	C	460–470
Spider	Australia	-16.742	126.089	I66	13	ex, smor	Sandstone	C	573
Roter Kamm	Namibia	-27.762	16.289	I67	2.5	ex, pc	Sandstone	S	5
Yilan	China	46.391	129.311	I69	1.85	ex, pc	Crystalline	S	0.05
Tswaing	SouthAfrica	-25.411	28.083	I70	1.13	ex, sub	Mixed	S	0.22
Shoemaker	Australia	-25.881	120.883	I71	30	ex, pc	Sandstone	C	1630
Brent	Canada	46.078	-78.482	I73	3.8	ex, pc	Crystalline	S	396–453
Ries	Germany	48.873	10.695	I77	26	ex, pc	Crystalline	C	15
Wolfe creek	Australia	-19.170	127.795	I78	0.88	ex, pc	Sandstone	S	0.12
Cleanskin	Australia	-18.170	137.942	I79	15	ex, pc	Sandstone	C	540–1400
Luizi	D.R. Congo	-10.175	28.006	I65	17	ex	Sandstone	C	575
Carswell	Canada	58.418	-109.517	I82	39	ex, smor	Mixed	C	481
Strangways	Australia	-15.200	133.567	I84	25–40	ex, pc	Mixed	C	646
Sao Miguel do Tapuio	Brazil	-5.617	-41.388	I87	21	ex	Sandstone	C	120
Amelia Creek	Australia	-20.858	134.883	I88	20	ex	Mixed	C	600–1600
Mistastin	Canada	55.891	-63.311	I89	28	ex, sub	Crystalline	C	36.6
Charlevoix	Canada	47.533	-70.350	I90	55	ex, sub	Mixed	C	450
Beaverhead	USA	44.600	-112.967	I91	60–75	ex, pc	Mixed	C	600
Araguainha	Brazil	-16.785	-52.983	I92	40	ex	Crystalline	C	252–259
Lawn Hill	Australia	-18.693	138.652	I93	20	ex, pc	Sandstone	C	472
Manicouagan	Canada	51.399	-68.683	I94	70–100	ex, sub	Crystalline	C	214
Liverpool	Australia	-12.393	134.047	I81	2	ex, pc	Sandstone	S	150
Tabun-Khara obo	Mongolia	44.131	109.654	I83	1.3	ex, pc	Sandstone	S	145–163
Ritland	Norway	59.249	6.422	I39	2.7	ex, pc	mixed	S	500–540
Aouelloul	Mauritania	20.241	-12.675	I45	0.39	ex, pc	Sandstone	S	3.1
Dalgaranga	Australia	-27.633	117.289	I56	0.024	ex, pc	Crystalline	S	0.27
Monturaqui	Chile	-23.928	-68.262	I58	0.36	ex	Crystalline	S	0.663
Kalkkop	SouthAfrica	-32.709	24.432	I55	0.64	ex, pc	Sandstone	S	0.25

Amguid	Algeria	26.088	4.395	I68	0.45	ex, pc	Sandstone	S	0.1
Kamil	Egypt	22.018	26.088	I19	0.045	ex	Sandstone	S	0.003
Boxhole	Australia	-22.613	135.196	I14	0.17	ex	Crystalline	S	0.017
Whitecourt	Canada	53.999	-115.596	I72	0.036	ex	Sandstone	S	0.001
Henbury	Australia	-24.571	133.148	I23	0.18	ex, pc	Sandstone	S	0.0042
Rio Cuarto	Argentina	-32.871	-64.183	I31	4.5	ex	Sandstone	S	0.11
Yallalie	Australia	-30.443	115.771	I59	12	pc	Sandstone	C	83.6–89.8
Presquile	Canada	49.726	-74.833	I74	22	ex, sub	Crystalline	C	500
Macha	Russia	60.085	117.652	I60	0.3	ex, pc,	Sandstone	C	0.0073
Rock Elm	USA	44.717	-92.228	I28	6.5	ex, pc	Sandstone	C	410–460
Mount Toondina	Australia	-27.945	135.359	I52	4	ex, pc	Sandstone	C	66 – 144
Kelly west	Australia	-19.933	133.950	I75	14	ex, pc	Sandstone	C	541
Matt Wilson	Australia	-15.506	131.181	I42	7.5	ex	Sandstone	C	1400–1500
Sudbury	Canada	46.600	-81.183	I76	180–200	ex, pc	Crystalline	C	1849
Vredefort	SouthAfrica	-27.009	27.500	I85	180–275	ex, pc	Crystalline	C	2023
Rochechouart	France	45.831	0.782	I86	23	ex	Crystalline	C	201
Yarrabubba	Australia	-27.183	118.833	I80	30	ex, pc	Sandstone	C	2246

C: Complex, S: Simple, T: Transitional, ex: exposed, pc: partial covered, smor: subdued morphology, sub: submerged

Table A2. Volcanic calderas used in this study were selected from collapse caldera worldwide database (CCDB) [30, 34].

Volcanic Calderas	Country	Latitude	Longitude	D_max	D_min	Type	ID
Toba	Indonesia	2.580	98.830	100	30	C	V103
Taal	Philippines	14.010	120.998	30	25	S	V10
Kawah Ijen	Indonesia	-8.119	114.056	20	20	S	V18
Ijen_II	Indonesia	-8.058	114.244	18	17	S	V19
Shikotsu	Japan	42.751	141.317	15	13	S	V49
Long Valley	USA	37.717	-118.884	32	18	C	V56
Solitario	USA	29.451	-103.809	16	16	C	V62
Rotorua	NewZeland	-38.080	176.250	20	16	S	V73
Crater Lake	USA	42.930	-122.113	10	8	S	V74
Henry's Fork Caldera	USA	44.330	-111.330	37	29	C	V77
Ngorongoro	Tanzania	-3.177	35.580	19	16	S	V80
Kapenga	NewZeland	-38.089	176.273	?	?	C	V92
Colli Albani	Italy	41.754	12.700	12	10	C	V97
Copahue	Chile& Argentine	-37.858	-71.177	10	10	S	V03
Paektu Mountain	China &N. Korea	42.005	128.056	14	12	S	V07
Karymshina	Russia	54.118	159.657	25	15	C	V101
Aso	Japan	32.885	131.084	25	18	C	V17
Mount Longonot	Kenya	-1.155	36.354	12	8	C	V37
Valles	USA	35.870	-106.570	22	16	C	V58

Braciano	Italy	42.316	12.174	20	15	S	V96
Akademia Nauk	Russia	53.981	159.462	11	11	S	V98
Uzon	Russia	54.500	159.970	12	9	C	V99
Ayarza	Guatemala	14.420	-90.120	7	5	S	V08
Mount Okmok	USA	53.468	-168.175	9.3	9.3	C	V09
Deriba	Sudan	12.950	24.270	5	5	C	V23
Toya	Japan	42.598	140.856	10	9	C	V48
Mount Silali	Kenya	1.152	36.231	8	5	C	V59
Ilopango	El Salvador	13.670	-89.050	11	8	C	V60
Alcedo	Ecuador	-0.430	-91.120	7.4	6.1	S	V67
Mount Aniakchak	USA	56.864	-158.151	10	10	C	V79
Emi Koussi	Chad	19.851	18.538	16	12	C	V93
Huichapan	Mexico	20.340	-99.550	10	10	C	V104
Sollipulli	Chile	-38.970	-71.520	4	4	S	V15
Gadamsa	Ethiopia	8.356	39.181	7	9	C	V24
Karkar	New Guinea	-4.650	145.967	5.5	3.2	C	V25
Agua de Pau	Portugal	37.770	-25.470	7	4	S	V26
The Barrier	Kenya	2.320	36.587	6	5	C	V29
Mallahle	Ethiopia	13.270	41.650	6	6	C	V34
Asavyo	Ethiopia	13.098	41.599	12	12	C	V35
Suswa	Kenya	-0.915	36.457	12	8	C	V36
Kone	Ethiopia	8.840	39.688	6	5	C	V40
San Pedro	Mexico	21.263	-104.698	8	8	C	V46
Gallosuelo	NewZeland	-5.200	151.240	?	?	S	V51
Darwin	Ecuador	-0.180	-91.280	5	5	S	V68
Cerro Azul	Ecuador	-0.170	-91.240	5	5	S	V69
Sierra Negra	Ecuador	-0.830	-91.170	10	7	S	V71
Worf	Ecuador	-0.020	-91.350	7	5	S	V72
Cerro Panizos	Argentina	-22.187	-66.681	15	15	C	V75
Gadamsa	Ethiopia	8.350	39.180	10	8	C	V76
Incapillo	Argentina	-27.902	-68.824	6	5	C	V78
Olmoti	Tanzania	-3.016	35.652	6.5	6.5	C	V82
Nemurt	Turkey	38.621	42.235	8.5	7	S	V91
Vico	Italy	42.120	12.230	-	-	C	V94
Montefiascone	Italy	42.579	11.931	3	3	S	V95
Laslajas	Nicaragua	12.300	-85.730	7	7	C	V04
Krasheninnikov	Russia	54.593	160.273	11	9	C	V102
Karthala	Comores Island	-11.760	43.353	4	3	S	V12
Ale Bagu	Ethiopia	13.508	40.632	3	2.1	C	V13
Amealco	Mexico	20.126	-100.169	11	11	C	V16

Numazawa	Japan	37.450	139.579	3	2	C	V22
Sete Cidades	Portugal	37.870	-25.780	5	5	S	V28
Fantale	Ethiopia	8.984	39.907	4	3	S	V39
Mauna Loa	USA	19.479	-155.603	6.2	2.5	C	V41
Fernandina	Ecuador	-0.370	-91.550	6.5	6.5	S	V70
Embagai	Tanzania	-2.911	35.827	4	4	S	V81
Gorely Khrebet	Russia	52.558	158.027	13	10	C	V87
Changbaishan	China & N. Korea	42.005	128.058	5	5	S	V05
Mount Katmai	USA	58.260	-154.975	10	10	S	V11
Towada IV	Japan	40.500	140.900	3.5	3	S	V21
Furnas	Portugal	37.770	-25.320	6	6	C	V27
Kaguyak	USA	58.613	-154.053	3	2.5	S	V31
Mazama	USA	58.613	-154.053	10	8	C	V38
Villarrica	Chile &Argentine	-39.420	-71.950	9	6	C	V53
Aoba (Ambae)	Vanuatu	-15.389	167.835	2.1	2.1	S	V02
Izu-Oshima	Japan	34.724	139.394	4.5	3.5	C	V06
Ngozi	Tanzania	-9.010	33.554	3	3	S	V30
Pinatubo	Philippines	15.142	120.350	2.5	2.5	S	V32
Cerro Azul	Chile	-35.653	-70.761	4	5	S	V33
Geger Halang	Indonesia	-6.896	108.408	4	4	C	V44
Ceboruco	Mexico	21.125	-104.508	3.7	3.7	C	V45
Mount Meru	Tanzania	-3.247	36.748	3.5	3.5	C	V52
Ikeda	Japan	31.237	130.561	5	4	C	V57
Coate peque	El Salvador	13.859	-89.553	5	5	C	V61
TianChi	China	42.007	128.054	5	5	S	V64
Tazawa	Japan	39.721	140.663	6	6	S	V65
Sakurajima	Japan	31.578	130.661	23	17	C	V01
Conguillio	Chile	-38.901	-71.728	4	3	S	V14
Paka	Kenya	0.918	36.191	1.5	1.5	S	V20
Mauna Kea	USA	19.813	-155.472	4.2	2.5	C	V42
Poas	Costa Rica	10.200	-84.233	2.5	2.5	S	V43
Kuttara	Japan	42.500	141.180	3	3	S	V47
Gallosuelo	NewZeland	-5.342	151.117	13	10.5	C	V50
Logo Tromen	Chile-Argentine	-39.931	-72.028	5	6	C	V54
Mocho chosheunco	Chile-Argentine	-39.500	-71.715	5	4	C	V55
Lake City	USA	37.955	-107.391	18	15	C	V63
Groppo	Ethiopia	11.715	40.232	3.8	3.8	C	V66
Monduli	Tanzania	-2.868	35.949	2.9	2.9	S	V83
Gela	Tanzania	-2.763	35.916	3.1	3.1	S	V84
Oldeani	Tanzania	-3.297	35.449	3	3	S	V85

Creede	USA	37.748	-106.922	25	20	C	V86
Mutnovsky	Russia	52.451	158.166	9	9	C	V88
Ksudach	Russia	51.800	157.530	7	7	C	V89
Opala	Russia	52.543	157.339	14	12	C	V90
Mary Semyachik	Russia	54.058	159.442	10	10	C	V100

C: Coalesced pit, S: Single pit, D_min: Minimum Diameter, D_max: Maximum diameter

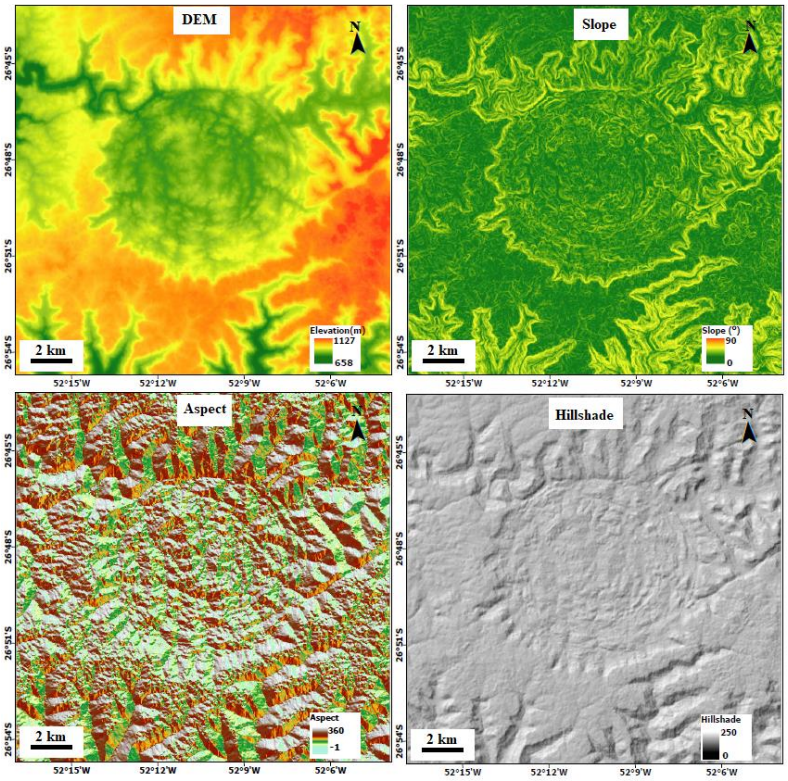

(a) Vargeão Dome impact crater, Brazil.

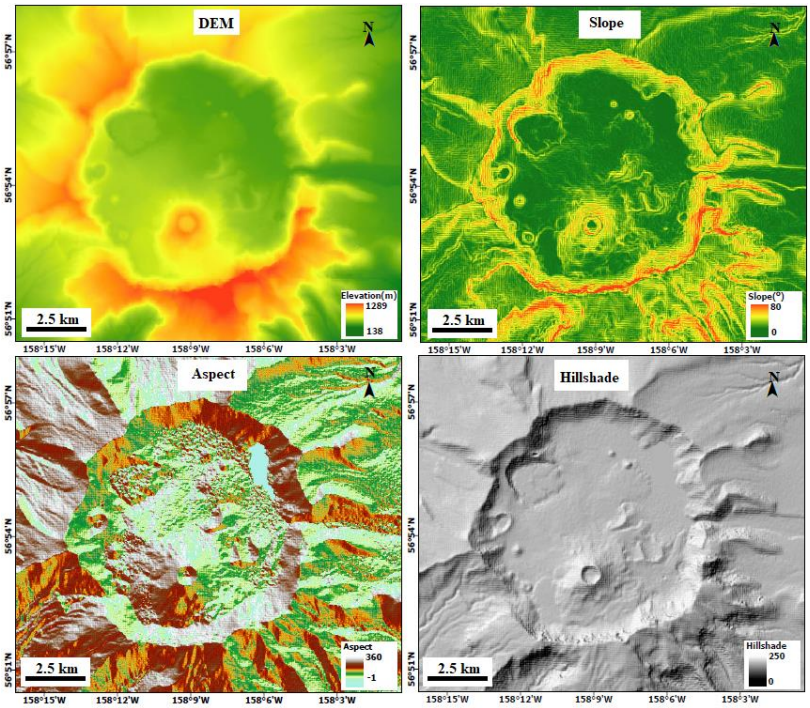

(b) Mount Aniakchak Caldera, USA

Figure A1. Representative examples of DEM, slope, aspect and hillshade layers for (a) impact crater and (b) Volcanic caldera used in segmentation.

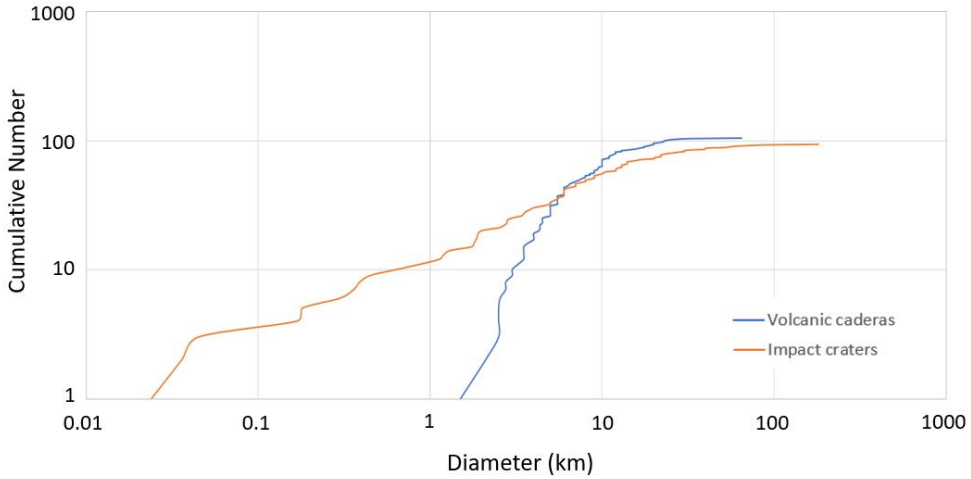

Figure A2. Size frequency distribution plot of impact craters and volcanic calderas used in this study.

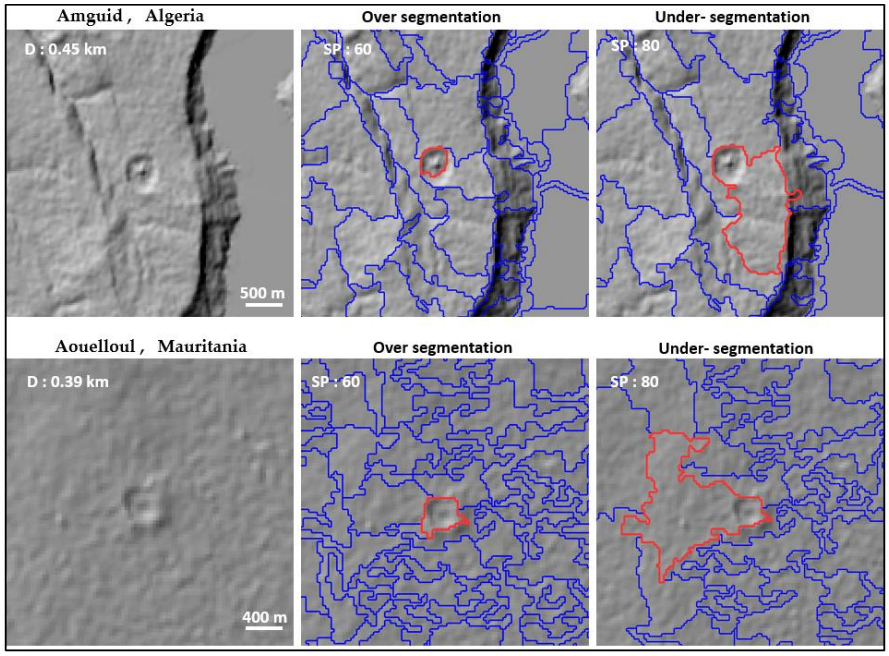

Figure A3. Representative segmentation of impact craters smaller than 0.88 km diameter showing unreliable segmentation results.

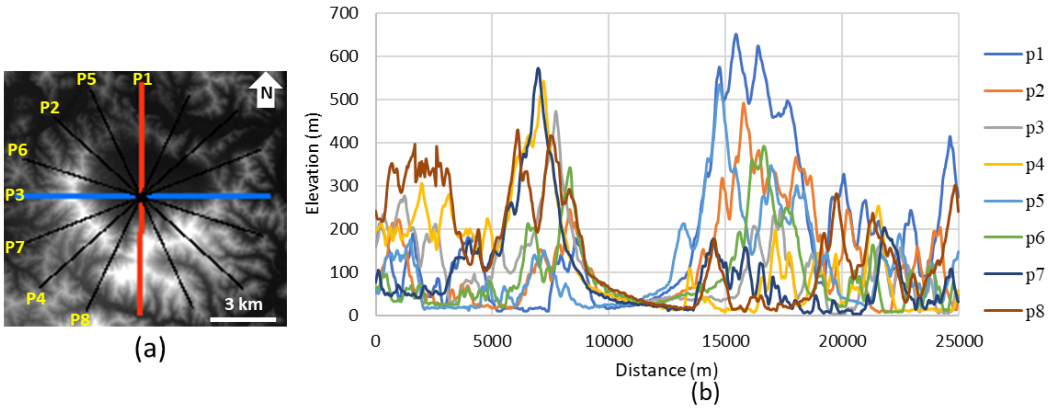

Figure A4. (a) Eight topographic profiles crossed JCB, (b) the stacked profiles of JCB, where p1-8 stand for topographic profiles.

Investigation of topographic and object characteristics of terrestrial impact craters based on remote sensing approaches

HABIMANA Emmanuel

Advisor Jaehyung Yu

Abstract

Impact craters provide inference on planet evolution, space materials, and are unevenly distributed worldwide due to limited advanced geological exploration in most developing countries. The eight optimal scale parameters from 80 to 3000 have been identified by multiple segmentation, area fitness index, and visual inspection. The relationship of scale parameters and impact crater size was indicated by a positive correlation (R^2=0.78) with rim diameter. The object-oriented classification using Random Forest have been applied to impact craters, volcanic calderas, and valleys, and detected terrestrial impact craters with an overall accuracy of 88.4% and Kappa coefficient of 0.8. The important variables indicated that the geometric attributes played the most role in detecting impact craters followed by topographic and textures attributes. The terrestrial impact craters, in general, have relatively lower circularity, higher length to width ratio, lower relief, slope, and elevation than volcanic calderas. Valley can be easily distinguished from the other features. The geological process of impact crater formation makes more vulnerable to surface erosion of rims and post-sediment deposition resulting lower circularity and topographic variation than volcanic calderas. The study also tested the applicability of morphometric parameters in defining impact crater type using statistical tests and machine learning algorithms. The training and validation datasets of data consisted of the

data from 52 confirmed, well preserved, and moderately eroded impact craters and a recently discovered impact crater in Korea, Jeokjung Chogye Basin (JCB). The Mann Whitney U test and One Sample Wilcoxon signed rank test statistics revealed that the morphometric parameters including rim diameter, wall width, floor diameter can statistically separate complex craters and simple craters. The classification assessment of simple and complex craters based on Random Forest model provided an overall accuracy of 88.6 % and a Kappa coefficient of 0.67. The classification efficiency is mainly driven by the crater size, where the complex craters are generally distinguished by the large rim diameter, flood diameter and wide wall width compared to simple craters with narrow parabolic bases which are mainly caused by impact energy level. The study confirmed that complex and simple craters can be distinguished by test statistics and machine learning algorithm and could be useful for impact craters with detectable rims. The classification method is only valid for simple and complex craters due to the small sample of transitional craters that are currently available of Earth. Therefore, this integrated approach using global elevation datasets could be effective approaches for detecting possible impact craters and defining their respective crater types at preliminary exploration stage thereby contributing to the new impact crater discoveries.

원격탐사 접근법을 기반으로 한 지상 충돌 분화구의 지형 및 물체 특성조사

하비마나 임마누엘

충남대학교 대학원 우주지질학과 우주지질학전공 (지도교수 유재형)

Korean Abstract

충돌 분화구는 행성 진화, 우주 물질에 대한 추론을 제공하며 대부분의 개발도상국에서 제한된 고급 지질 탐사로 인해 전 세계적으로 고르지 않게 분포되어 있습니다. 80 에서 3000 까지의 8 가지 최적 척도 매개변수는 다중 분할, 면적 적합도 지수 및 육안 검사를 통해 식별되었습니다. 스케일 매개변수와 충격 크레이터 크기의 관계는 림 직경과 양의 상관관계 (R^2=0.78)로 나타났습니다. Random Forest 를 활용한 객체지향 분류는 충돌 분화구, 화산 칼데라, 계곡에 적용되었으며 전체 정확도 88.4%, 카파 계수 0.8 로 육상 충돌 분화구를 감지했습니다. 중요한 변수는 기하학적 속성이 충격 크레이터를 감지하는 데 가장 많은 역할을 했으며 지형 및 질감 속성이 뒤따랐음을 나타냅니다. 일반적으로 육지 충돌 분화구는 화산 칼데라보다 상대적으로 원형도가 낮고, 길이 대 너비 비율이 높으며, 기복, 경사 및 고도가 낮습니다. 밸리는 다른 지형지물과 쉽게 구별될 수 있습니다. 충돌 분화구 형성의 지질학적 과정은 테두리의 표면 침식과 퇴적 후 퇴적에 더 취약해 화산 칼데라보다 원형도와 지형 변화가 더 낮습니다. 또한 이 연구에서는 통계 테스트와 기계 학습 알고리즘을 사용하여 충격 분화구 유형을 정의할 때 형태학적 매개변수의 적용 가능성을

테스트했습니다. 데이터의 훈련 및 검증 데이터세트는 확인되고, 잘 보존되고, 적당히 침식된 52 개의 충돌 분화구와 최근 한국에서 발견된 충돌 분화구인 적중초계분지(JCB)의 데이터로 구성되었습니다. Mann Whitney U 테스트와 One Sample Wilcoxon 부호 순위 테스트 통계를 통해 림 직경, 벽 폭, 바닥 직경을 포함한 형태학적 매개변수가 복잡한 크레이터와 단순한 크레이터를 통계적으로 구분할 수 있음이 밝혀졌습니다. Random Forest 모델을 기반으로 한 단순 크레이터와 복잡한 크레이터의 분류 평가는 88.6%의 전체 정확도와 0.67 의 카파 계수를 제공했습니다. 분류 효율성은 주로 분화구 크기에 의해 결정됩니다. 여기서 복잡한 분화구는 주로 충격 에너지 수준으로 인해 발생하는 좁은 포물선형 바닥을 가진 단순한 분화구에 비해 큰 테두리 직경, 홍수 직경 및 넓은 벽 폭으로 일반적으로 구별됩니다. 이번 연구에서는 테스트 통계와 기계 학습 알고리즘을 통해 복잡하고 단순한 크레이터를 구별할 수 있으며 테두리가 감지되는 충돌 크레이터에 유용할 수 있음을 확인했습니다. 분류 방법은 현재 지구에서 사용할 수 있는 전이 크레이터의 작은 샘플로 인해 단순 크레이터와 복잡한 크레이터에만 유효합니다. 따라서 전 지구 고도 데이터세트를 활용한 통합 접근법은 예비 탐사 단계에서 충돌 가능성이 있는 충돌구를 탐지하고 각각의 충돌구 유형을 정의함으로써 새로운 충돌 분화구 발견에 기여하는 효과적인 접근 방식이 될 수 있습니다.